Pontifícia Universidade Católica
do Rio de Janeiro

Lesslie Katherine Guerra Jorquera

Detecting infrared radiation with QWIPs beyond the Bandoffset limit

PhD Thesis

Thesis presented to the Programa de Pós-Graduação em Engenharia Elétrica da PUC–Rio as partial fulfillment of the requirements for the degree of Doutor em Engenharia Elétrica

Adviser : Prof. Patrícia Lustoza de Souza
Co–Adviser: Prof. Mauricio Pamplona Pires

Rio de Janeiro, December 17, 2015

Pontifícia Universidade Católica
do Rio de Janeiro

Lesslie Katherine Guerra Jorquera

Detecting infrared radiation with QWIPs beyond the Bandoffset limit

Thesis presented to the Programa de Pós-Graduação em Engenharia Elétrica da PUC–Rio as partial fulfillment of the requirements for the degree of Doutor em Engenharia Elétrica. Approved by the following commission:

Prof. Patrícia Lustoza de Souza
Adviser
Departamento de Engenharia Elétrica — PUC–Rio

Prof. Mauricio Pamplona Pires
Co–Adviser
Departamento de Engenharia Elétrica — PUC–Rio

Prof. Enrique Victoriano Anda
Departamento de física — PUC-Rio

Prof. Gustavo Soares Vieira
IEAv-CTA

Prof. Paulo Ségio Soares Guimarães
UFMG

Prof. Roberto Jakomin
UFRJ-Xerém

Prof. Germano Maioli Penello
UERJ

Prof. Márcio da Silveira Carvalho
Coordinator of the Centro Técnico Científico da PUC–Rio

Rio de Janeiro, December 17, 2015

Lesslie Katherine Guerra Jorquera

Graduated in Physics at Pontifical Catholic University of Chile in 2008. Msc in Theoretical Physics at Pontifical Catholic University of Chile in 2011.

Bibliographic data

Guerra, Lesslie

Detecting infrared radiation with QWIPs beyond the Bandoffset limit / Lesslie Katherine Guerra Jorquera; adviser: Patrícia Lustoza de Souza; co–adviser: Mauricio Pamplona Pires. — Rio de Janeiro : PUC–Rio, Department of Engenharia Elétrica, 2015.

v., 72 f: il. ; 29,7 cm

Tese (doutorado) - Pontifícia Universidade Católica do Rio de Janeiro, Departamento de Engenharia Elétrica, 2015.

Inclui bibliografia.

1. Engenharia Elétrica – Tese. 2. QWIPs. 3. Fotodetectores. 4. Superrede. 5. Infravermelho. I. Lustoza de Souza, Patricia. II. Pamplona Pires, Mauricio. III. Pontifícia Universidade Católica do Rio de Janeiro. Departamento de Engenharia Elétrica. IV. Título.

CDD: 621.3

To my mother

Acknowledgments

I would like to thank my family for their unconditional support, my dear sister Dorka, my father Roberto, my stepfather Darwin and especially the person that I admire the most, who always has been giving me support and love, who has been my inspiration, my mother Vinskovita. I would like to thank Victor, who has believed in me even when I doubted.

To all my friends, the people who made these years unforgettable, especially Gidy, Vane, Daniela and Daniel, who have always been with me giving me their support and friendship.

To all the people in LabSem, not only for their help in academia, but also for doing of LabSem a friendly place to work. Thanks to Germano, for always been there willing to help me with my endless questions. And especially I would like to thank my advisers Patricia Lustoza and Mauricio Pires, who were my guides in this PhD but they also were someone I can always count on, thank for their patience with me, for always being willing to help everyone in the lab and thank them mostly for keeping the lab as a gratifying and pleasant place to work.

I would like to thank everyone who helped in the different stages of this thesis, to the professors Marcelo Maialle and Marcos Degani from UNICAMP, to professor Alain Quivy from USP, to Totó Von Zuben from UNICAMP and everyone from CBPF.

Finally, I want to thank CNPq, FAPERJ and PUC-Rio for the granted aid, without which this work could not be done.

Abstract

Guerra, Lesslie; Lustoza de Souza, Patricia (Advisor); Pamplona Pires, Mauricio (Co-Advisor). **Detecting infrared radiation with QWIPs beyond the Bandoffset limit**. Rio de Janeiro, 2015. 72p. PhD Thesis — Departamento de Engenharia Elétrica, Pontifícia Universidade Católica do Rio de Janeiro.

III-V semiconductors are extensively investigated for fabrication of quantum well infrared photodetectors (QWIPs); however the operation wavelength is limited by the bandoffset of the materials allowing infrared transitions for wavelength larger than 3.1 μm. For wavelength shorter than 1.7 μm band to band transitions are easily employed. Thus, in III-V QWIPs, the range between 1.7 and 3.1 μm cannot be reached either by band-to-band or by intraband transitions. In this thesis a specially designed superlattice structure is proposed in order to detect radiation within this forbidden range. The structure proposed consists of a superlattice with a wider central quantum well, which generates a modulation in the continuum creating minibands and minigaps for energies above the bottom of the conduction band of the quantum well, including in the continuum. With this approach the limitation of having bound states only with energies below the barrier no longer holds and it is possible to detect energies higher than the limit imposed by the bandoffset of the materials. Theoretical simulations for the structure were performed and absorption, dark current, and photocurrent measurements were carried out showing peaks at 2.1 μm, in close agreement with the theoretically expected value.

Keywords

QWIPs; Photodetectors; Superlattices; Infrared.

Resumo

Guerra, Lesslie; Lustoza de Souza, Patricia; Pamplona Pires, Mauricio. **Detecção de radiação infravermelho com QWIPs além do limite do Bandoffset**. Rio de Janeiro, 2015. 72p. Tese de Doutorado — Departamento de Engenharia Elétrica, Pontifícia Universidade Católica do Rio de Janeiro.

Os semicondutores III-V são amplamente investigados para a fabricação de fotodetectores de infravermelho baseados em pontos quânticos (QWIPs); no entanto, o comprimento de onda de operação é limitada pelo bandoffset dos materiais que permitem transições de infravermelho de comprimento de onda maior que 3,1 μm. Para comprimentos de onda mais curto do que 1,7 μm transições banda a banda são facilmente empregadas. Assim, em QWIPs III-V, o intervalo entre 1,7 e 3,1 μm não pode ser alcançado tanto por transições banda-banda ou por transições intrabanda. Nesta tese uma estrutura de superrede especialmente desenhada é proposta a fim de detectar a radiação dentro desta faixa proibida. A estrutura proposta consiste numa superrede com um poço quântico central mais amplo, o qual gera uma modulação no contínuo criando minibandas e minigaps para energias acima da parte inferior da banda de condução do poço quantico, incluindo no contínuo. Com esta abordagem, a limitação de ter estados ligados apenas com energias abaixo a barreira não se mantém e é possível detectar energias mais elevadas do que o limite imposto pelo bandoffset dos materiais. Simulações teóricas para a estrutura foram realizados e medidas de absorção, corrente de escuro, e fotocorrente foram realizadas mostrando picos em 2,1 μm, em estreita concordância com o valor teoricamente esperado.

Palavras–chave

QWIPs; Fotodetectores; Superrede; Infravermelho.

Contents

List of Figures

1
Introduction

Infrared photodetectors have a wide range of applications in different areas such as telecommunication, environmental monitoring, infrared vision, industrial security, and military, among others, for this reason they are extensively studied nowadays.

For the fabrication of the photodetectors, semiconductors II-VI and III-V are commonly used. Among the detectors based on II-VI semiconductors, the most important to be mentioned is HgCdTe (also known as MCT) which can operate in the range of 0.8 to 25 μm and it was first produced by Lawson, Nielsen, Putley and Young [2]. The disadvantages of this type of photodetectors II-IV are the problems in their production, its high cost in growth and processing and their non-uniformity over large area, which creates difficulties in the production of large area devices such as the Focal Plane Arrays. Since III-V do not have these problems they could be better material choice.

The aim of this thesis is the study of photodetectors based on quantum wells, QWIPs (Quantum Well Infrared Photodetectors). The quantum wells are created when we join different semiconductors (with its different band energy), in an epitaxial growth. A material of smaller gap is grown between materials of larger gap, confining the electrons and holes in a potential well. By controlling the thickness of the well, on the nanometre order, we can tune the optical transitions of the structure.

When a QWIP is illuminated with radiation it absorbs a photon and an electron is excited, potentially leading to the production of photocurrent with the same energy as the energy of the transition. There are two types of transitions: interband, involving transitions between the conduction band and the valence band, and intraband, involving transitions between quantized levels in the conduction band or valence band. Figure 1.1 shows the two types of transitions present QWIPs.

The interband transitions are limited by the band gap of the materials used. In the intraband there are different types of transitions, however all of them are also limited by the band offset of the materials, making it impossible to obtain transition energies higher than the energy of the barrier (determined by the materials used).

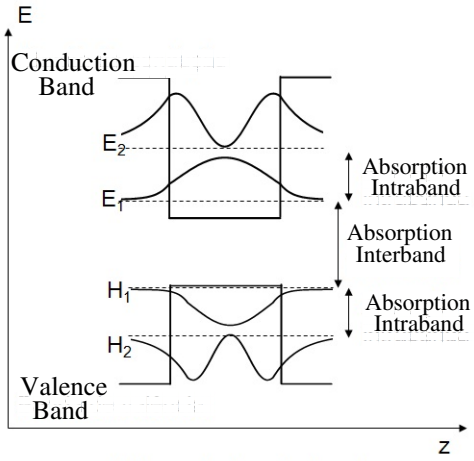

Figure 1.1: Types of QWIPs transition: interband and intersubband

Then, the operation energies when using intraband transitions in III-V semiconductors are limited to energies below 400 meV. For energies above 700 meV interband transitions are easily employed. Thus, in QWIPs based on III-V semiconductors there is a "forbidden gap", a range between 400 and 700 meV (1.7-3.1 μm), that cannot be reached either by interband or by intraband transitions in regular QWIPs.

In this work, another type of configuration, in order to achieve this forbidden energy range, is proposed. A set of quantum wells forming a superlattice allows generating a modulation in the continuum and creates minigaps and minibands that grant us a better control over the energy levels. Then a defect, in the otherwise periodic superlattice, is introduced by inserting a well with a larger thickness than that of the other wells in the superlattice, with this we create bound states within the minibands. Previous reports have shown infrared photodetection for 300 meV using similar structures [3].

This proposed configuration not only will allow achieving higher energy, exceeding the limits imposed by the band offset, but also, obtain a high selectivity and a good electron extraction, important in the generation of photocurrent.

In the next chapter a theoretical background, that will help us to have a better understanding of the photodetectors, is shown. Then, in chapter 2, the experimental procedures required for the fabrication and later tests of the performance of the QWIPs are explained in detail. In chapter 3 the results of the theoretical simulations and experimental measurements are exhibited and analysed. Finally the conclusions of the work are presented.

2
Theoretical framework

In this chapter, a theoretical background that allows the development of photodetectors based on intraband transitions in quantum wells is shown. The production and the performance of such devices are described and analised in the next chapter.

First, a brief and general theoretical review about the photodetectors is presented, and then, a more specific theory for the photodetectors based on quantum wells is carried out.

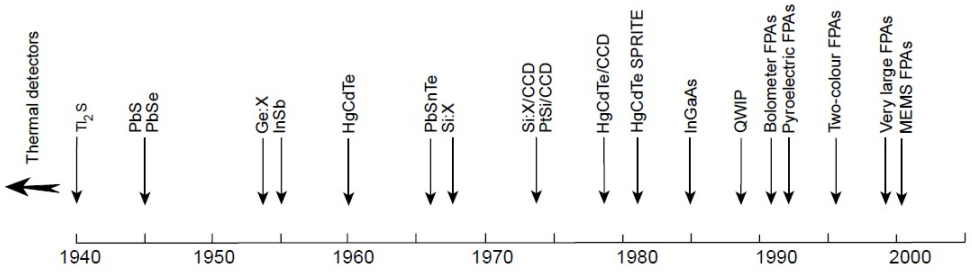

Figure 2.1: Timeline of the infrared photodetectors development [1]

2.1 General theory of infrared photodetectors

The first observation of infrared radiation was made by Herschel [4] in 1800, using in his experiment a thermometer as a detector. But it was only in the XX century when the photodetectors were developed and was in 1917 when Case [5] developed the first infrared photoconductor. The history of the development of infrared photodetectors [1] is shown in figure 2.1.

There are different types of photodetectors, a comparison list of the advantages and disadvantages [1] is presented in figure 2.2. The thermal detectors are based on the change of some physical property of the material, due to a change in the temperature when the incident radiation is absorbed, to generate an electrical output. Some detectors of this type are: thermopile [6], bolometers [7] and pytoelectric.

In this work we are interested in the second type of detectors, the photon detectors, which, depending on the nature of the interaction, can be divided in: intrinsic, extrinsic, free carriers, quantum well and quantum dots, figure 2.2. Specifically, in this thesis photodetectors based on quantum wells are investigated.

2.2 QWIPs

2.2.1 Basic concepts

Lets begin with the basic theoretical concepts that are necessary to understand the functioning of a QWIP.

- **Quantum well**

A potential quantum well is a region in space where the electrons feel a lower potential than the one in the barrier. Unlike what happens in the classical

Comparison of infrared detectors

Detector type			Advantages	Disadvantages
Thermal (thermopile, bolometers, pyroelectric)			Light, rugged, reliable, and low cost Room temperature operation	Low detectivity at high frequency Slow response (ms order)
Photon	Intrinsic	IV–VI (PbS, PbSe, PbSnTe)	Easier to prepare More stable materials	Very high thermal expansion coefficient Large permittivity
		II–VI (HgCdTe)	Easy bandgap tailoring Well developed theory & exp. Multicolour detectors	Non-uniformity over large area High cost in growth and processing Surface instability
		III–V (InGaAs, InAs, InSb, InAsSb)	Good material & dopants Advanced technology Possible monolithic integration	Heteroepitaxy with large lattice mismatch Long wavelength cutoff limited to 7 μm (at 77 K)
	Extrinsic (Si:Ga, Si:As, Ge:Cu, Ge:Hg)		Very long wavelength operation Relatively simple technology	High thermal generation Extremely low temperature operation
	Free carriers (PtSi, Pt_2Si, IrSi)		Low-cost, high yields Large & close packed 2-D arrays	Low quantum efficiency Low temperature operation
	Quantum wells	Type I (GaAs/AlGaAs, InGaAs/AlGaAs)	Matured material growth Good uniformity over large area Multicolour detectors	High thermal generation Complicated design and growth
		Type II (InAs/InGaSb, InAs/InAsSb)	Low Auger recombination rate Easy wavelength control	Complicated design and growth Sensitive to the interfaces
	Quantum dots	InAs/GaAs, InGaAs/InGaP, Ge/Si	Normal incidence of light Low thermal generation	Complicated design and growth

Figure 2.2: Comparasion of infrared detectors [1]

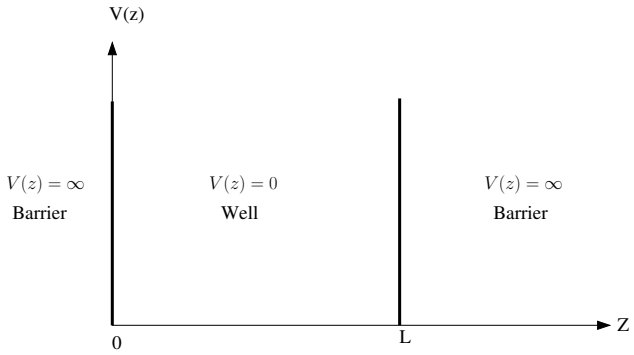

Figure 2.3: Infinite potential well

regime, in the quantum counterpart the electrons inside the potential barrier are distributed in discrete energy levels. The Schrödinger equation [8] describes the behavior of the wavefunction in the system

$$i\hbar\frac{\partial}{\partial t}\psi(\vec{r},t) = \hat{H}\psi(\vec{r},t) \tag{1}$$

where $\hat{H} = \frac{-\hbar^2}{2m}\nabla^2 + V(\vec{r},t)$ is the system Hamiltonean, ψ the wavefunction, $\hbar = \frac{h}{2\pi}$ the reduce Planck's constant and m the mass of the particle.

• Infinite potencial well

Lets consider the 1D quantum well time independent Schrödinger equation with infinite potential barriers, as shown in figure 2.3:

$$-\frac{\hbar}{2m}\frac{d^2\psi}{dz^2} + V(z) = E\psi, \tag{2}$$

where E is the energy of the system and $V(z)$ is the function describing the potencial energy, that in the case of an infinite potencial well is

$$V(z) = \begin{cases} 0 & : 0 < z < L, \\ \infty & : \text{otherwise.} \end{cases} \tag{3}$$

Inside the well ($0 < z < L$) there is no potencial, which means that the particle has the same behavior of a free particle, thus, the solution for the wavefunction in the well is

$$\psi(z) = A\sin(kz) + B\cos(kz), \tag{4}$$

with $k = \frac{\sqrt{2mE}}{\hbar}$. Imposing continuity in $\psi(0) = \psi(L) = 0$ and normalizing we obtain

$$B = 0, \tag{5}$$

$$|A|^2 = \frac{2}{L}, \tag{6}$$

$$k_n = \frac{n\pi}{L}, \quad \text{with } n = 1, 2, 3, 4... \tag{7}$$

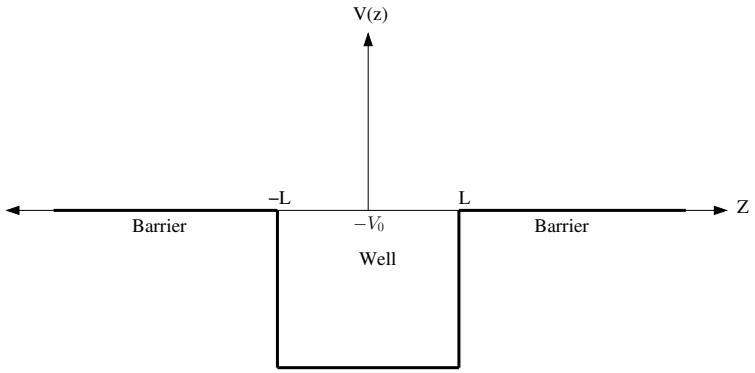

Figure 2.4: Finite potential well

Then, the solution of the Schrödinger equation is

$$\psi(z) = \sqrt{\frac{2}{L}} \sin\left(\frac{n\pi z}{L}\right), \tag{8}$$

and we also obtain the energies

$$E_n = \frac{\hbar^2 k_n^2}{2m} = \frac{\pi^2 \hbar^2}{2mL^2} n^2. \tag{9}$$

With this result we now can see clearly the difference from the classical case. If we think in a classical system, where an object is trapped inside a box, the object can move freely at any speed through the entire box, and there is not any preferencial place where we can find it. However, in the quantum system, we can see from equation 8 that the particle is more likely to be found at certain positions than others and also exist some positions in which the electron could not be found. Additionally, from equation 9 we can conclude that the energy is quantized, i.e., the electron can only occupy certain energy levels.

• **Finite potential well**

If now we consider finite barrier, as shown in figure 2.4, the potencial is given by

$$V(z) = \begin{cases} 0 & : |z| > L, \\ -V_0 & : -L \leq z \leq L. \end{cases} \tag{10}$$

and the solution of the Schrödinger equation give us the wavefunction

$$\psi(z) = \begin{cases} Be^{\kappa z} & : z < -L, \\ C\sin(lz) + D\cos(lz) & : -L \leq z \leq L, \\ Fe^{-\kappa z} & : z > L, \end{cases} \tag{11}$$

with,

$$\kappa = \sqrt{\frac{-2mE}{\hbar}}, \tag{12}$$

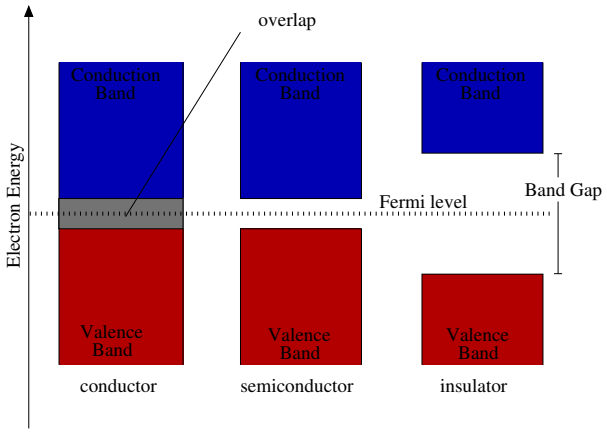

Figure 2.5: Band gap

$$l = \frac{\sqrt{2m(E+V_0)}}{\hbar}. \tag{13}$$

If we think in a classical system where a particle has less total energy than the barriers it is impossible to find the particle outside the box. However, with this example, we can see that in a quantum system there is a non-zero probability of finding the particle outside the box, even if the total energy of the particle is lower than the one of the barriers, this penetration in the barrier is going to be very important in the comprehension and analysis of the structures that we are going to consider on in this thesis.

2.2.2 Electronic band structure

As was briefly explained in the introduction and shown in the previous examples, in quantum systems there are ranges of energies that an electron in a solid can have, called energy band, and some ranges that it can not have, called band gaps, wich are described by the band structure of the solid.
In a semiconductor the conduction band, the lowest energy band that has unoccupied states, and the valence band, the highest energy band that contains electrons, are separated by a band gap, as shown in figure 2.5. When we talk about the band gap, in the case of semiconductors, we are referring to the energy difference that exists between the top of the valence band and the bottom of the conduction band. If an electron absorbs a photon it can be excited from the valence band to the conduction band.
The band gap at room temperature of some important materials for this thesis are: GaAs 1.43 eV, AlAs 2.16 eV, InP 1.35 eV and InAs 0.36 eV. Other materials are shown in figure 2.6.

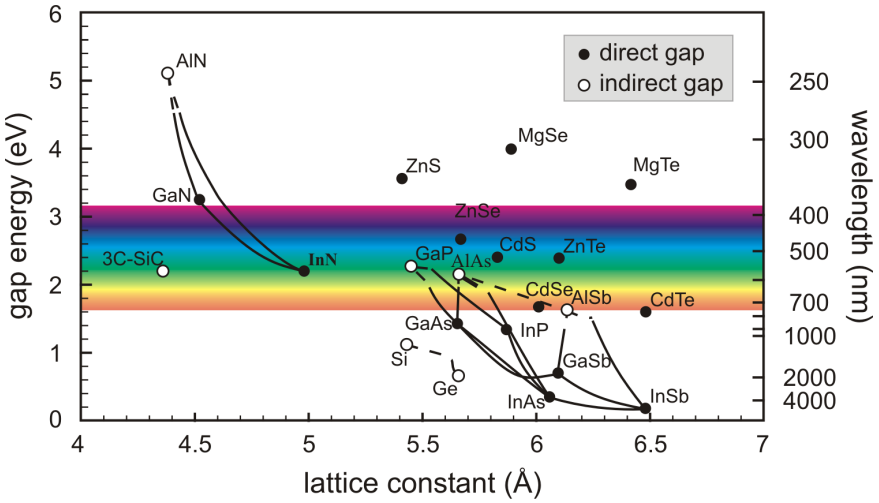

Figure 2.6: Band gap and lattice constant of some materials at 300K

• **Carriers distribution**

The energy distribution of the carriers, in this case fermions (electrons), is given by the Fermi-Dirac distribution

$$f(E) = \left[1 + e^{\frac{E-E_f}{k_b T}}\right]^{-1}, \tag{14}$$

where E_f is the system Fermi energy, k_b the Boltzman constant and T the system temperature. With this distribution, the electron concentration in the conduction band can be calculated [9]

$$n = \int_{E_c}^{\infty} D(E) f(E) dE \tag{15}$$

with E_c being the energy at the bottom of the conduction band and $D(E)$ the density states that, in our system, is

$$D(E) = \frac{m}{\pi\hbar^2} \sum_i H(E - E_i), \tag{16}$$

where the heaviside function is $H(x) = 1$ for $x > 0$ and $H(X) = 0$ for $x < 0$. It can be noticed that the carrier concentration (15) depends only on the system temperature.

2.2.3 Stark effect

In order to collect the carriers and generate a photocurrent a bias voltage must be applied to the sample. When we apply this bias, we modify the potencial of the system, as shown in figure 2.7. If a static electrical field E

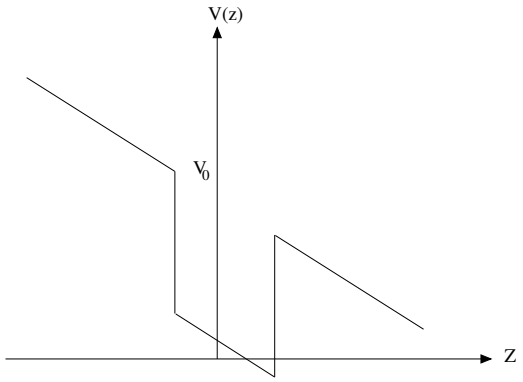

Figure 2.7: Potential with a static electric field applied

is applied in the perpendicular direction of the well plane, the potencial is then given by

$$V = V_0 - eEz. \tag{17}$$

where e is the electron charge. The field modifies the conduction band, tilting the potential along the Z axis.

In order to solve the equation, the perturbation theory is used and the wave function and energies found are

$$E_n = E_n^{(0)} + H'_{nm} + \sum_{m \neq n} \frac{|H'_{nm}|^2}{E_n^{(0)} - E_m^{(0)}}, \tag{18}$$

$$\begin{aligned} \psi_n &= \phi_n^{(0)} + \sum_{m \neq n} \frac{H'_{nm}}{E_n^{(0)} - E_m^{(0)}} \phi_m^{(0)} \\ &+ \sum_{m \neq n} \left[\sum_{k \neq n} \frac{H'_{mk} H'_{kn}}{(E_n^{(0)} - E_m^{(0)})(E_n^{(0)} - E_k^{(0)})} - \frac{H'_{mn} H'_{nn}}{(E_n^{(0)} - E_m^{(0)})^2} \right] \\ &- \frac{|H'_{mn}|^2}{2(E_n^{(0)} - E_m^{(0)})^2} \phi_n^{(0)}, \end{aligned} \tag{19}$$

where

$$H'_{nm} = \int \phi_n^{(0)}(z)(-eEz)\phi_m^{(0)}(z)dz \tag{20}$$

is the coupling term of the wavefunction of the original Hamiltonean with the field.

2.2.4 Light coupling in intraband transitions

The process of generating a photocurrent strongly depends on the absorption of the sample, for this reason we are going to look a little deeper into this phenomenon.

With an incident light on the sample, a photon can be absorbed and thereby

excite an electron, which will go from a lower to a higher energy level. The probability that a photon will be absorbed depends on the polarization of the incident photons and on specific established selection rules. To calculate the absorption probability we consider the Hamiltonian H [10] composed by an undisturbed part of a quantum well $H_0 = \frac{\vec{p}^2}{2m} + V(\vec{r})$ and a part that represents the time-dependent perturbation due to the incident light H' is [11]

$$H' \simeq -\frac{e}{m}\vec{A}\cdot\vec{p}, \tag{21}$$

with $\vec{A}$ being the potential vector of the electromagnetic field

$$\vec{A} = \hat{e}A_0\cos(\vec{k}\cdot\vec{r} - \omega t), \tag{22}$$

where $\vec{k}$ is the wave vector, ω the angular frequency of the incident light and $\hat{e}$ the unitary vector in the direction of the optical field. With this, the Hamiltonian H' can be rewritten as

$$H'(\vec{r},t) = H'(\vec{r})e^{-i\omega t} + H'^{+}(\vec{r})e^{i\omega t}, \tag{23}$$

where

$$H'(\vec{r}) = -\frac{eA_0e^{i\vec{k}\cdot\vec{r}}}{2m}\hat{e}\cdot\vec{p}. \tag{24}$$

The probability of a photon being absorbed and a electron being excited from the state $|a\rangle(n,\vec{k}_t)$ to the state $|b\rangle(n',\vec{k}'_t)$, in a dipole aproximation, is

$$\Gamma_{a\to b} = \frac{2\pi}{\hbar}\frac{e^2}{2m}|\langle b|\vec{A}\cdot\vec{p}|a\rangle|^2\delta(E_b - E_a - \hbar\omega), \tag{25}$$

that can be rewriten in terms of the dipole momentum $\vec{u}_{ba}$ of the transition $b \to a$

$$\Gamma_{a\to b} \simeq \frac{2\pi}{\hbar}(-\vec{u}_{ba}\cdot\vec{E})^2\delta(E_b - E_a - \hbar\omega), \tag{26}$$

where $\vec{E}$ is the potencial field define in $\vec{A}$.

Thereby, the selection rules can be defined when we find the dipole momentum $\vec{u}_{ba}$

$$\begin{aligned}\vec{u}_{ba} &= e\langle b|\vec{r}|a\rangle \\ &= e\langle b|x|a\rangle\hat{x} + e\langle b|y|a\rangle\hat{y} + e\langle b|z|a\rangle\hat{z}.\end{aligned} \tag{27}$$

In the case of quantum wells, the dipole momentum only has components in the direction $\hat{z}$ (growth direction), then $\vec{u}_{ba} = e\langle b|z|a\rangle\hat{z}$, so it is the component $\hat{z}$ that allows the electron transition to higher energies and thus absorption.

To obtain a transition between states $|b\rangle$ and $|a\rangle$ the condition (25) must be fulfilled

$$H'_{ba} = \langle b|H(\vec{r})|a\rangle \neq 0, \tag{28}$$

that is, in terms of the dipole,

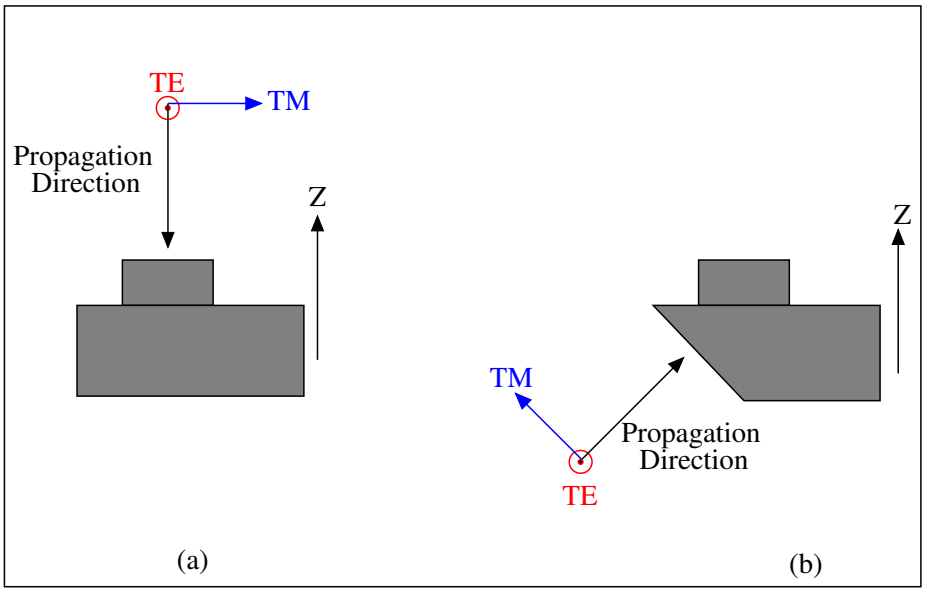

Figure 2.8: Schematic of incident radiation on the sample

$$H'_{ba} = \langle b|\frac{-e}{m}\vec{A}(\vec{r})\cdot\vec{p}|a\rangle = -\vec{u}_{ba}\cdot\vec{E} \neq 0. \quad (29)$$

If the electric field does not have a component in $\hat{z}$, then, from equation 27 and 29 we have $H'_{ba} = 0$, i.e, we do not have absorption. This is why we need to modify the geometry of the grown sample so that the incident radiation arrives with at least a component of the electric field in the z direction. The sample will be polished at an angle of 45, so the radiation can be coupled with our device.

Figure 2.8 shows a scheme of how the incident radiation reaches the sample at different angles. In 2.8-a the light reaches parallel to the sample (to the growth direction), and the field has no component in the Z axis, then the light is not coupled with the QWIP and we have no absorption. However, if we polish the sample at 45 degrees as shown in the 2.8-b, TM has a component in the Z direction, thus we obtain a coupling between the radiation and our QWIP, consequently absorption occurs.

2.2.5 Types of QWIPs

As explained in general terms in the introduction, there are different types of QWIPs. There are different configurations for the possible intraband transitions, depending on the type of transition it can be: bound to bound, bound to continuum or bound to quasi-bound.

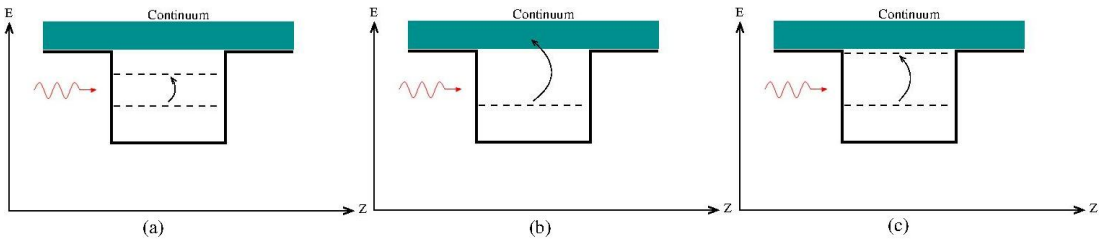

Figure 2.9: Types of transitions: (a) bound-bound, (b) bound-continuous, (c) bound-quase ligado

• **Bound-Bound**

A transition bound to bound B-B, (figure 2.9a) is a transition between two bound states inside the quantum well. Adjusting some parameters such as the thickness of the well, two states are obtained in the well, the transition B-B is the one from the ground state to the first excited state. The advantages of this approach are the high selectivity that can be achieved, the narrow peak absorption and the high oscillator strength, but the disadvantage is the low electron extraction since the excited electron is still confined in the quantum well. To remove the electron from an excited state and thereby generate a photocurrent, another process is required, like assisted tunneling or thermal excitation. The first B-B QWIP was shown by Levine in 1987 [12].

• **Bound-Continuum**

Another type of transition is bound to continuum B-C (figura 2.9b), these are transitions between a bound state in the quantum well and the continuum of extended states above the barrier. This approach is not very selective since there are many states above the barrier leading to a broad absorption peak. The main advantage of this configuration is the good electron extraction, since the electron is excited to an extended state, and easily collected to generate photocurrent. The first B-C QWIP was shown by Levine in 1988 [13].

• **Bound-Quasi-Bound**

Finally, we have the transitions bound to quasi-bound B-QB (figure 2.9c), this approach aims to get the best of the two previous approaches, it has good selectivity (not as good as the limit for bound) and a good electronic extraction (also not as good as the limit for continuum). The disadvantage is that, as the excited state must match the energy barrier, there is a very limited tuning.

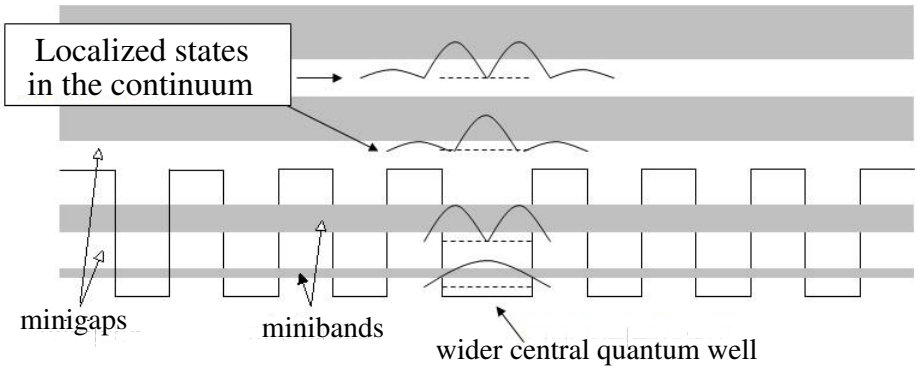

Figure 2.10: Superlattice. The central well has a thickness larger than the lateral wells acting as a defect in the periodic superlattice and generating localized states in the barrier and the continuum.

• **Superlattices**

In the basic configurations mentioned above the transitions are limited by the bandoffset of the materials, all operation energies need to be lower than the barriers of the quantum wells. In order to achieve higher operating energies we used superlattices (SL). The SL generate a modulation in the continuum, creating minigaps and minibands of energies between the bottom of the conduction band of the quantum well and the barrier, and in the continuum as well, which allows to have a control of the energy levels. As the miniband is an extended state, we have a good electron extraction, and the absorption peak is not as wide as the one in a transition bound to continuum.

The approach we are interested in this thesis is the one that uses a defect in the superlattice, for instance introducing a well with a larger thickness creating a defect in the periodic superlattice, producing bound states inside the quantum well and also in the continuum. These bound states in the continuum are also called Bragg-confined states [14, 15, 16] minigap-confined states [17, 18].

With this approach the limitation of having bound states with energies below the barrier is no longer needed, so we can study structures that allow to achieve higher transition energies than the limit imposed by the bandoffset of the materials. We have a high selectivity since the transitions are between bound states, an easy electronic extraction (similar to the transition bound to quase bound), a versatile tuning and an increase in the transition energy (which is no longer limited by the bandoffsets). Figure 2.10 shows a superlattice with a central well wider than the thickness of the lateral wells, and the minigaps, minibands and localized states created by it.

2.3 Basic elements of the theoretical model used in the simulations

The theoretical model used in the simulations solves the Schrödinger equation by performing the time evolution of the wave function and obtaining the energy levels for different structures [19]. The time evolution of the wave functions was done with the split-operator method, applied for both real and imaginary parts. The former gives the wave function time evolution and the latter gives the eigenvalues and eigenstates of the system.

The evolution of the wave function by one infinitesimal time increment Δt is given by

$$\Psi(\mathbf{r}, t + \Delta t) = e^{-iH\Delta t/\hbar}\Psi(\mathbf{r}, t), \tag{30}$$

with the Hamiltonian

$$H = T + V(\mathbf{r}), \tag{31}$$

where T is the kinetic energy operator and V the potencial energy operator.

As the operation in the equation (30) cannot be calculated exactly we need to use some approximations to evolve the wave function. There are several approximations that can be made. In the model used in this work, a procedure known as split-operator, method where we split the exponential operator as products of other exponentials, is performed.

Considering the exponential operator of the term with the Hamiltonian

$$\begin{aligned} e^{-iH\Delta t/\hbar} &= e^{-i(T+V)\Delta t/\hbar} \\ &= e^{-iV\Delta t/\hbar}e^{-i\mathbf{P}^2\Delta t/2\hbar m^*} + O(\Delta t^2) \\ &= e^{-iV\Delta t/2\hbar}e^{-i\mathbf{P}^2\Delta t/2\hbar m^*}e^{-iV\Delta t/2\hbar} + O(\Delta t^3) \\ &= e^{-iaV\Delta t/2\hbar}e^{-ia\mathbf{P}^2\Delta t/2\hbar m^*}e^{-iV\Delta t/2\hbar}e^{-ia\mathbf{P}^2\Delta t/2\hbar m^*}e^{-iaV\Delta t/2\hbar} + O(\Delta t^4), \end{aligned} \tag{32}$$

where $a = (3 + i\sqrt{3})/6$ and m^* is the effective mass within the one band model. As the kinetic and potential operators are not commutable an error is introduced in the terms $O(\Delta t^n)$, but as the operators are unitary they preserve the norm of the wave function and thus guarantee the conservation of probability and the unconditional stability of the method.

To propagate the wave functions, the numerical simulation use this split-operator method, repeating the calculations by infinitesimal time steps and obtaining also the eigenstates and eigenvalues for different structures.

This approximation can be used with different boundary conditions and the same scheme of propagation described above can be used to obtain the energy spectrum and the corresponding wave functions for a given potential.

3
Experimental techniques

This chapter describes the experimental techniques used to fabricate the samples and subsequent production of the photodetectors.
In addition, a description of the techniques used for the characterization of the photodetectors, such as x-ray diffraction, absorption and photocurrent, is presented.
The samples were grown in a Metalorganic Vapour Phase Epitaxy equipment for metal organic vapor gases (MOVPE), then the grown samples are processed to fabricate the device. After processing, the samples are mounted in a chip and electrical contacts are made to perform characterization measurements.

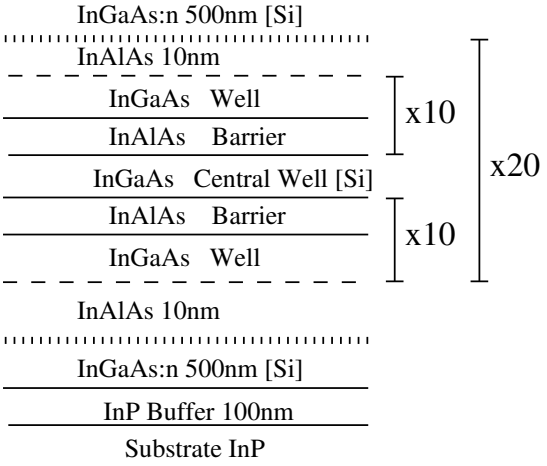

Figure 3.1: Sample structure

3.1 Samples growth

The samples used in this thesis were grown in the reactor of the LABSEM (Laboratorio de Semiconductores) of PUC-Rio, using Metalorganic Vapour Phase Epitaxy (MOVPE), an epitaxial crystal growth technique used for growing high quality single crystalline thin films of different materials on different substrates. MOVPE is based on the transport of chemical species in gaseous form to a growth chamber where they react and then the solid material is deposited on a monocrystalline substrate at high temperatures (600 to 700^{o}C) on which the gases decompose by pyrolysis.
As mentioned in the introduction the materials chosen were InGaAs wells and InAlAs barriers matched to an InP substrate. The structure consists of a twenty period SL with a wider central quantum well (CQW) in the otherwise periodic structure. This modified SL is itself reapeated twenty times (figure 3.1). The CQW is n-doped with Si to $2 \cdot 10^{18} cm^{-3}$, the whole active layer is sandwiched between two n-doped contact layers with the same doping levels as the CQW.

3.2 X Ray Diffraction

An important measurement in the process of characterization is the technique of x-ray diffraction, with which some information on the deposited layer such as: the crystalline quality, the lattice parameter and the layer thickness can be obtained. This is a non destructive technique that consists in focusing a x-ray beam on the sample and studying the interference of the reflected beam in the crystalline planes of the sample, as shown in figure 3.2.

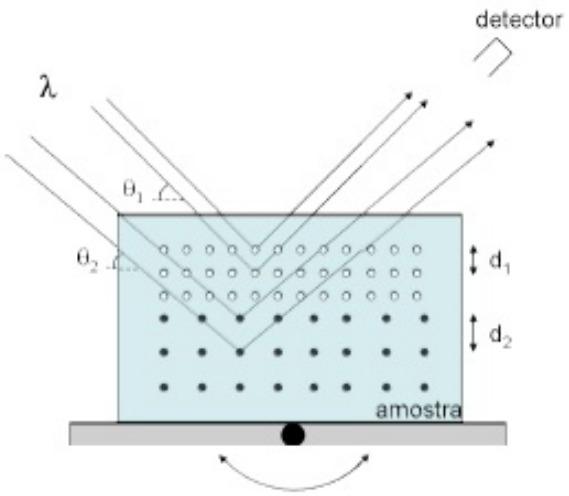

Figure 3.2: X-ray diffraction measure scheme

From the Bragg diffraction experiment we have [20]

$$n\lambda = 2\sin\theta \tag{1}$$

where λ is the wavelength of the incident x-ray, d the distance between the crystalline planes, n the diffraction order and θ the incident angle. A constructive interference condition can be obtained between the rays reflected in the crystal planes of the sample. The diffracted intensity is measured as a function of the angle in detail around the Bragg peak, the resulting profile is known as Rocking Curve.

For a sample with a simple structure, e.g., a crystalline layer on an InP substrate, the experiment shows two peaks, the peak of the substrate and the peak of the layer, as shown in figure 3.3. If we had only one peak, it means that the lattice parameter of the material coincides with that of the substrate and the single peak will be the superposition of the diffraction of both.

Given the equation [21],

$$\frac{\delta d}{d} = -\delta\theta cot\theta, \tag{2}$$

the lattice parameter difference can be obtained from the angular difference between the diffraction peaks δd and, since the lattice parameter of the InP substrate is known, the lattice parameter of the deposited layer can be obtained.

With this measurement the thickness of the deposited layer can also be obtained from the Pendellosung fringes [22]. The fringes occur only when the lattice parameter of the substrate is mismatched with the substrate parameter since they are formed due the interference between the beams diffracted by the substrate and the deposited layer at different angles. The spacing between

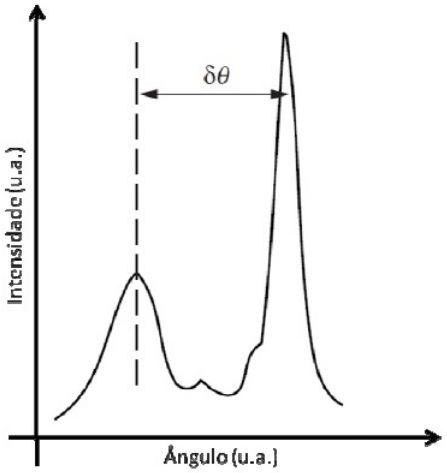

Figure 3.3: Example of a measurement of diffraction X-rays

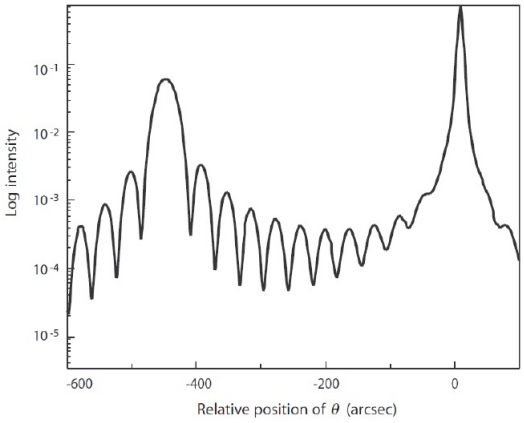

Figure 3.4: Pendellosung fringes example

the fringes is related to the thickness of the sample through [23]

$$\Delta\theta_p = \frac{\lambda\gamma_g}{tsin2\theta}, \tag{3}$$

where $\gamma_g = sin\Psi$, with Ψ being the angle between the diffracted beam and the surface of the crystal. An example of Pendellosung fringes is shown in figure 3.4, we see that the layers of the sample and the substrate are mismatched. This measurement is very important for the growth calibration, since we use alloys we need to determine the composition of the materials. Figure 3.5 shows one of the samples grown for the calibration. It consists of a layer of InGaAs on an InP substrate. Through the x-ray experiment the composition could be determined, 52.8% of In and 47.2% of Ga.

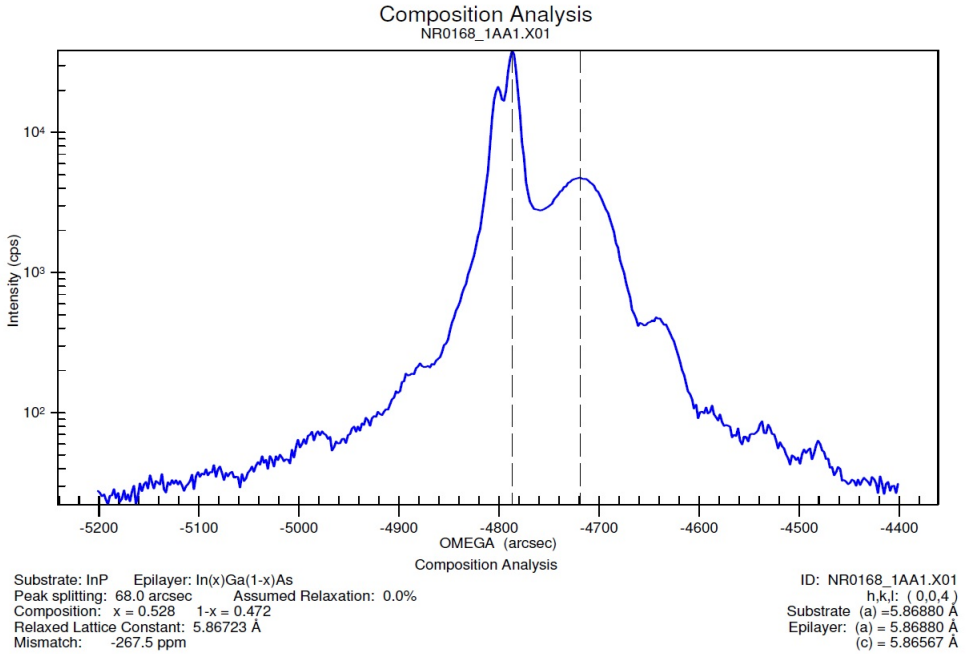

Figure 3.5: X ray sample NR0168

3.3 Absorption

The absorption is a very important measurement because it allows to verify if the samples present a peak absorption in accordance with the theoretical wavelength expected.

The measurements were carried out with Fourier transform infrared spectroscopy (FTIR). Perpendicular incident radiation does not couple to intraband transitions in QWIPs, as explained in the previous chapter, for this purpose, the grown samples are polished to produce a 45 degree coupling facet on which light is focused at normal incidence. Additionally, this waveguide geometry allows multiple reflections of the beam inside the sample, increasing the interaction of radiation with the quantum wells and, therefore, the absorption itself.

The basic principle of FTIR consists of an infrared source which emits a beam that is divided by a beam splitter, the resulting beams enter a Michelson interferometer and the difference is plotted on an interferogram, then a software applies the inverse fourier transform and plots the intensity absorbed as function of the wavelength. The measurements are made at room temperature in a closed chamber which is purged with dry air to remove CO_2 absorptions.

Figure 3.6: Equipment used for polishing the samples at 45 degrees

3.3.1 Polish at 45 degrees

To obtain a sample polished at 45 degrees, first the sample is fixed to an aluminum piece as the one shown in figure 3.6, so that it remains at the desired angle. Once the sample is fixed on the support we begin with a gross polish, performed with a water sandpaper number 2500, then a finer polish is made with alumina of 2 μm and finally one with alumina 0.2 μm is performed. The sample surface, on the grown side, is already polished; however on the substrate side it is not, so a plane polishing must be made on that side, with the support shown in figure 3.6.

3.3.2 Setup

The polished sample is placed in the support shown in figure 3.7 (a), which is then placed into the FTIR according to the configuration shown in figure 3.7 (b). The polarizer is used to filter the TE or TM polarized light.
As the polarization TE is not absorbed in intraband transitions it will be used as a reference. Thus, when we calculate ln(TE/TM) we are removing all contributions that do not come from absorption by the quantum wells. In addition, we are removing the background by doing the subtraction of the ln(TE/TM) measured without sample.

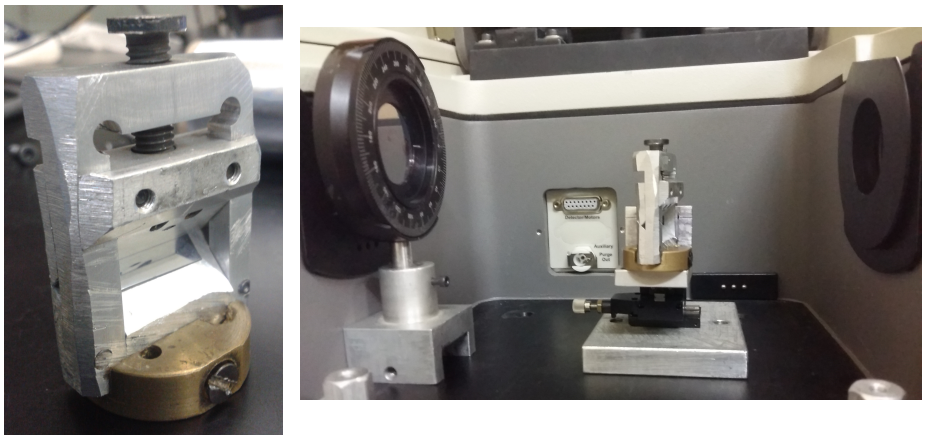

(a) (b)

Figure 3.7: (a) Support for sample at 45 degrees, (b) Absorption setup

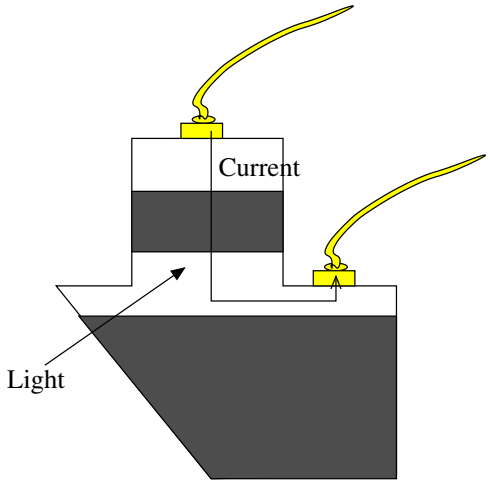

Figure 3.8: Current direction on the device

3.4 Photodetectors production

In order to produce a QWIP the grown sample has to be processed to obtain a device that allows the collection of the generated current.
For the electron confined in the quantum well we need that the current flows in the direction of the growth, as shown in figure 3.8. To accomplish this we must corrode the sample to reach the first layer and bond an electrical terminal. The steps that must be followed to produce the device are (figure 3.9):
(a) Cleaning of the grown sample.
The sample is cleaned with the solvents trichloroethylene (TCE), acetone and isopropyl alcohol (IPA), then dried with nitrogen gas (N_2) and finally is

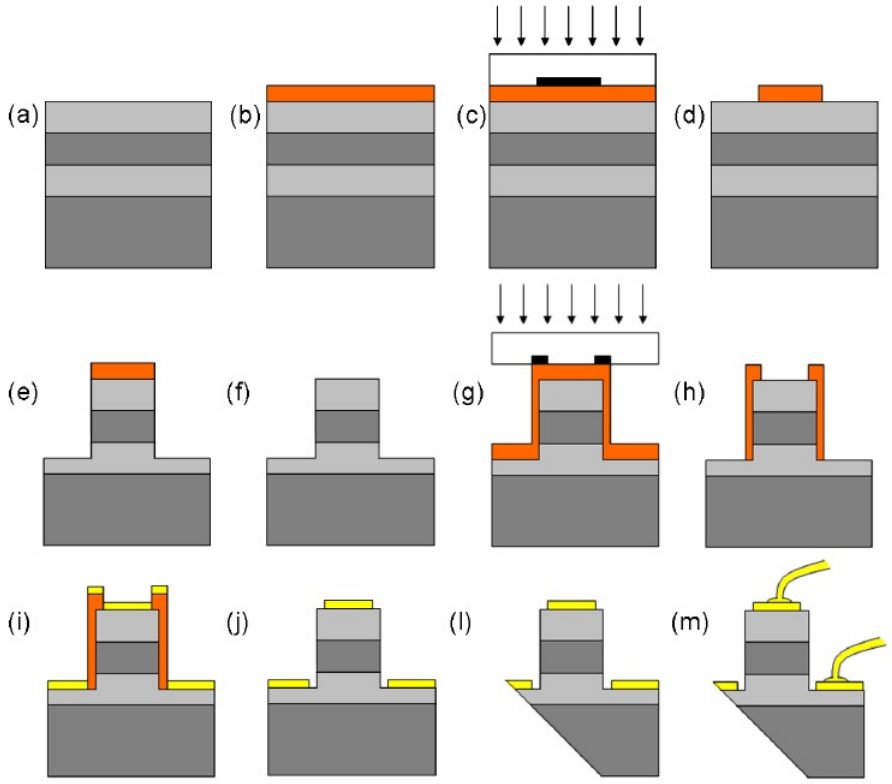

Figure 3.9: Processing phases: (a) final clean sample, (b) photoresist application, (c) selective illumination, (d) developing (e) corrosion, (f) cleaning, (g) photoresist and selective illumination, (h) developing, (i) metalization, (j) cleaning, (l) 45^o polish, (m) gold wires bond

heated in a hot plate to remove the humidity of the sample surface that could disrupt the adhesion of photoresist.

(b) Spin coating.

A ultraviolet photosensitive resin (photoresist AZ5214) is spread on the sample with the spinner, then the sample is heated in the hot plate at 110^oC for 2 minutes to harden the fotoresist.

(c) Photolithography.

For the exposure, the sample is placed in the Karl Suss MJB3 equipment, aligned with the masks (figure 3.10) and then selectively illuminated by ultraviolet light. After this step the pattern of the mask is recorded in the fotoresist on the sample.

(d) Developing.

The photoresist illuminated by UV is removed using the developer solution AZ400 and then the sample is heated at 120^oC for 10 minutes.

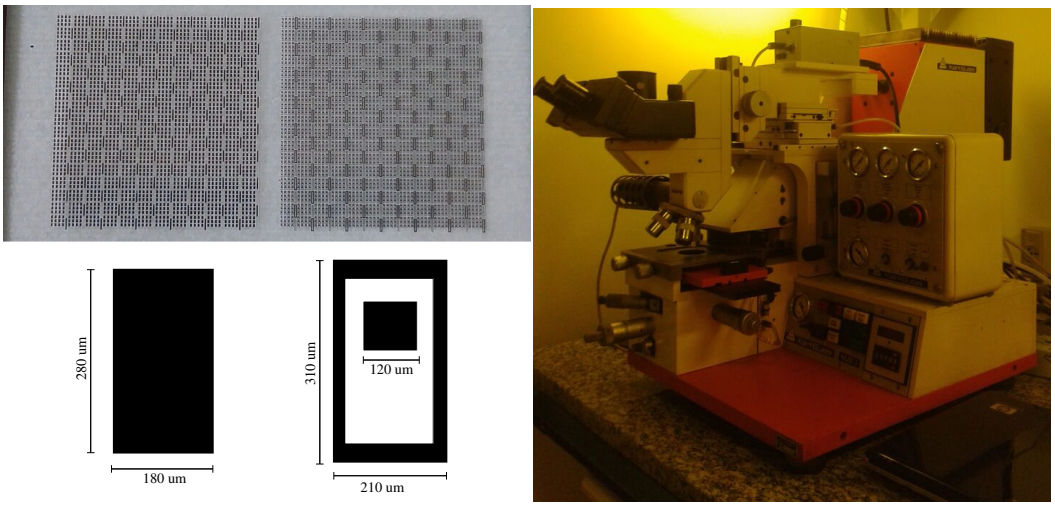

Figure 3.10: Mask alingner and mask used in photolithography

(e) Etching.
The sample is corroded with a solution of $H_2SO_4 : H_2O_2 : H_2O$ (1:8:40), this solution provides a corrosion rate of 1μ/min.
(f) Cleaning.
The photoresist is removed by cleaning the sample with TCE, acetone and IPA.
(g) Second litography.
Photoresist is put in another region of the sample and illuminated.
(h) Developing.
The illuminated photoresist is removed with AZ400.
(i) Metalization.
For this step the sample is introduced in the metal evaporator machine, shown in figure 3.11. Titanium and gold are evaporated to obtain a layer of 15 and 200 nm respectively, this will allows to make the ohmic contacts.
(j) Lift off.
The sample is immersed in acetone to remove the metal from the unwanted regions.
(l) Polish.
As explained at the previous section, the sample is polished at 45^o.
(m) Contacts.
Finally the sample is placed on a chip and the contact is made. To make the contact the bonding machine, shown in figure 3.12, is used to bond the gold wires from the sample to the chip.
After these steps the device is then ready for the characterization measurements.

Figure 3.11: Metal evaporator machine. Unicamp, Campinas, Brazil

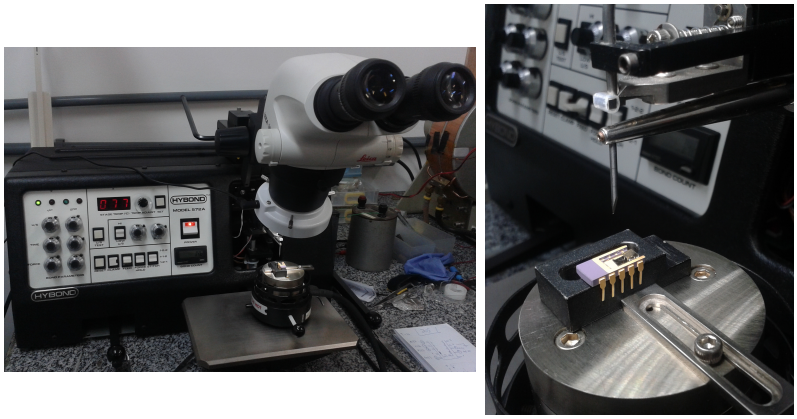

(a) (b)

Figure 3.12: Bonding machine. CBPF, Rio de Janeiro, Brazil

3.5 Dark current and background

We want to measure the electrical response of QWIP to the incidence of light (photocurrent), but there is a current generated by the carriers in the dark (dark current), which is not generated by light radiation but by the device itself. The dark current in QWIPs is widely studied in the literature and comes from several factors: at low temperature (< 90K) is dominated by direct tunneling through the barrier between neighboring wells, at high temperature (> 90K) depends on the thermally assisted tunneling and thermionic excitation processes that depend on the states of the continuum. Then, we need to measure this background since it is a limiting condition for the photodetector. In order to measure only the dark current the sample is placed in complete darkness wrapped in a heat shield at the same temperature. Bias voltage is applied on the sample and current at different temperatures is measured.

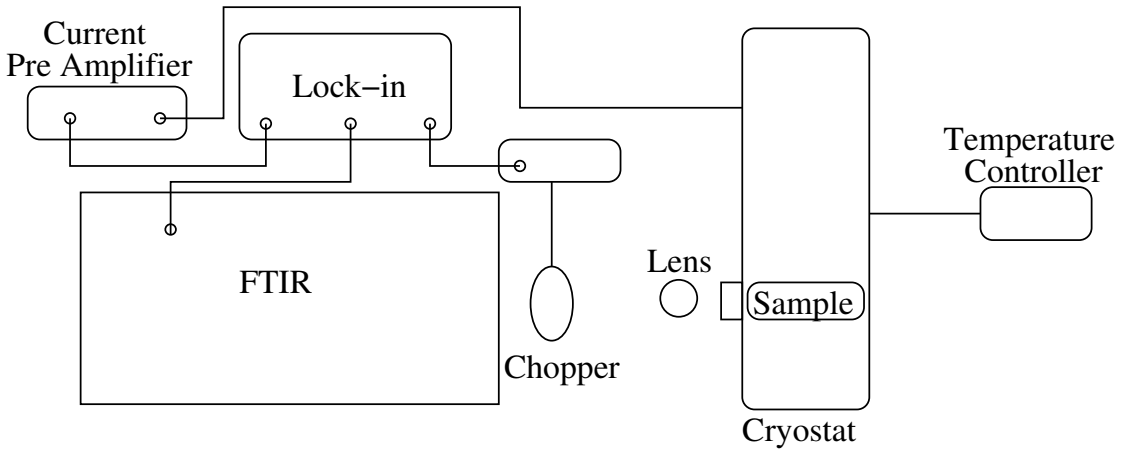

Figure 3.13: Photocurrent setup

3.6 Photocurrent

This measurement technique determines the current generated by the incident light on the sample. The experiment consists in illuminating the sample, applying an electric field in the direction of growth to accelerate electrons generated by the incident light, and measure the photocurrent.

We aim to verify if it has generated a peak in the same absorption wavelength measured previously. The absorption peaks may not necessarily have equivalent peaks in photocurrent, since the photocurrent not only depends on the absorption, but also on the electronic extraction. For example, if an electron is excited from a bound state to another bound state, both inside the quantum well, it may not contribute to the current because it requires some other mechanism to leave the well to the continuum and be collected to generate current.

However, by applying an electric field on the sample we modify its band structure and thereby we increase the probability of the electron tunneling through the barrier and contribute to the photocurrent, this effect is known as Fowler-Nordheim tunneling or field induced tunneling [24]. The closer to the top of the barrier the bound state is, the higher the probability of tunneling, that is why it is often desired to work with QWIPs with transitions between bound and quasi-bound states [25].

In order to perform this experiment the setup shown in figure 3.13 is used. This measurement was carried out at Labsem, PUC-Rio with a FTIR (Fourier Transform Infrared) model Thermo Nicolet 8700. A simple scheme of the FTIR operation is shown in figure 3.14.

Infrared energy is emitted from a source which is inside the FTIR (figure

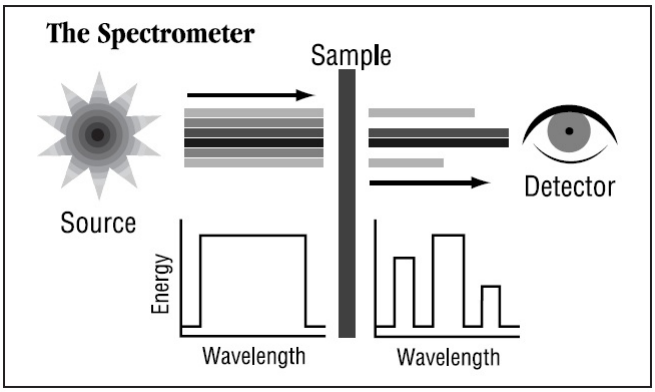

Figure 3.14: FTIR

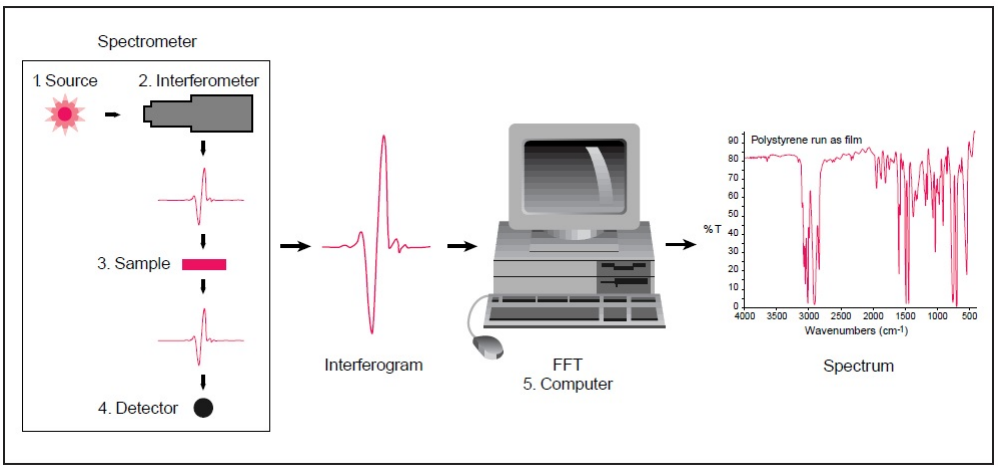

Figure 3.15: FTIR

3.15), as explained in section 3.3. Specific frequencies are absorbed by the sample, depending on its structure, and a current is generated. The resulting interferogram is finally digitized and sent to the computer for analysis, where the software uses the inverse Fourier transform to obtain the final spectrum.
For the purpose of achieving a good alignment and minimizing the noise, a chopper is placed in the path of the beam and the voltage detected by a pre amplifier is sent to a Lock-in. In spite of it, the measurement relies heavily on the alignment, therefore, the intensities of each measurement can not be directly compared if they were performed in different situations.
The sample is placed in a cryostat, this allows to have a control on the temperature. First, for a first set of samples, the cryostat model DE-202 (with a compressor model ARS-4HW) was used, which decreases the temperature through a compressor and allows to achieve temperatures as low as 20K. Then, for a second set of samples, the Janis cryostat was used, that allows to lower the temperature until 77K (liquid nitrogen temperature).

Another parameter that can be varied is the applied voltage on the sample, the control is done by the current amplifier HP 4145B. With this we can obtain the photocurrent generated by the sample at different temperatures and applied voltages and consequently study its behavior.

4
Results and discussion

In this chapter the results of the different experiments performed are presented. First, the simulations that have been made to decide the samples to grow in order to reach the transitions with the desired energy are explained; then, the processed samples and the finished devices are exhibited. Finally, the results of the experiments such as absorption, dark current and photocurrent are shown and analysed.

4.1 Theoretical simulations

In order to decide which structures of the samples should be grown, first simulations were performed to calculate the energy levels of the structures and thereby choose the ones that present transitions at the desired energy.

In the simulations, the Schrödinger equation is solved for the potential designed, obtaining the eigenstates and eigenvalues, i.e., the wave functions and their energies. These simulations were performed with a numerical method [19] by M. Degani and M. Maialle, professors at Unicamp-Limeira with whom we have a collaboration. This method solves the Schrödinger equation within the effective mass approximation with a modified version of a split-operator approach to propagate the wave functions by infinitesimal time steps.

In addition to the eigenvalues and eigenstates, with this method we calculated the oscillator strength and the transmission, which allows us to obtain the absorption spectra.

First we consider a structure consisting of a CQW of 8 nm of thickness, LQW of 2 nm and a barrier of 3 nm and, to study in more detail this structure, two other samples with a small variation in the thickness of the barrier were grown, varying it from 2 nm to 3 nm and 4 nm. The results of simulations of such structures are shown in Figures 4.1, 4.2 and 4.3.

On the left side of the figures the band structure of the samples with the probability density for the different states obtained from simulations are shown, marked in green and blue (depending on the parity) the bound states formed by the design of the structure are exhibited. We also see that minigaps and miniband are formed inside the quantum well and above it, as expected with the use of superlattices.

On the right side of the figures we have the absorption obtained by the simulations, the blue curve represents the absorption from the transitions from the ground state and the green curve the transitions from the first excited state.

In principle, only transitions from the ground state (blue curve) are possible since this is the only populated state, then, as the first excited state should not be populated the absorption from it (green curve) will not be observed experimentally.

From the selection rules it is known that the only transitions allowed are between states with different parity [26], then from the ground state we only have transitions to the first excited state and third excited state (states with odd parity above them are also allowed but would have a weaker oscillator strength).

The first absorption peak we see (blue curve) comes from a transition between

the ground state and the first excited state, this is the absorption with strongest oscillator strength, however this transition should not generate photocurrent since after the transition the electron is still trapped inside the quantum well.

The second absorption peak comes from a transition from the ground state to the third excited state. Although it has a weaker oscillator strength this transition could generate photocurrent since after the transition the electron is no longer trapped inside the quantum well and, by applying a bias we tilt the miniband above the third excited state allowing the electron to generate photocurrent.

From the simulations we observe that the structure with a barrier of 3 nm has a transition between the ground state and the third excited state with energy approximately of 566 meV, which exceeds the band offset limit. The structure with a barrier of 2 nm shows an absorption at an energy of 608 meV and the one with a barrier of 4 nm an energy of 518 meV. Then, by decreasing the thickness of the barriers the transition energy between the ground state and the third excited state will increase.

To achieve even higher transition energies we simulate other structure decreasing the thickness of the CQW to 7 nm and that of the LQW to 1.5 nm. Figure 4.4 shows the probability densities and the energy levels of this structure. In order to study in more detail this structure other two samples were grown varying the thickness of the barrier to 2nm (figure 4.5) and 4 nm (figure 4.6). As opposed to the previous samples, these three new samples present the second excited states outside the quantum well. However, since the transition from the ground state to this state is not allowed, this should not affect the absorption or photocurrent that the samples will generate.

We obtain from the simulations that the structure with a barrier of 3 nm has a transition between the ground state and the third excited state with an energy approximately of 621 meV, the one with a barrier of 4 nm an energy of 565 meV and the one with a barrier of 2 nm present the highest energy observed among all the simulated samples, 697 meV.

As in the previous three samples, we notice that by increasing the barrier thickness we decrease the energy transition. In principle, when we move the third excited state away from the miniband we would need to apply a higher bias to generate photocurrent, but the absorption should not vary.

We observe that varying the thicknesses of the wells of the barriers we achieve a control over the bound states, the minibands and the minigaps and, therefore we can attain higher energies than the bandoffset limit, as expected with the use of superlattices, thereby increasing the detection range of the material.

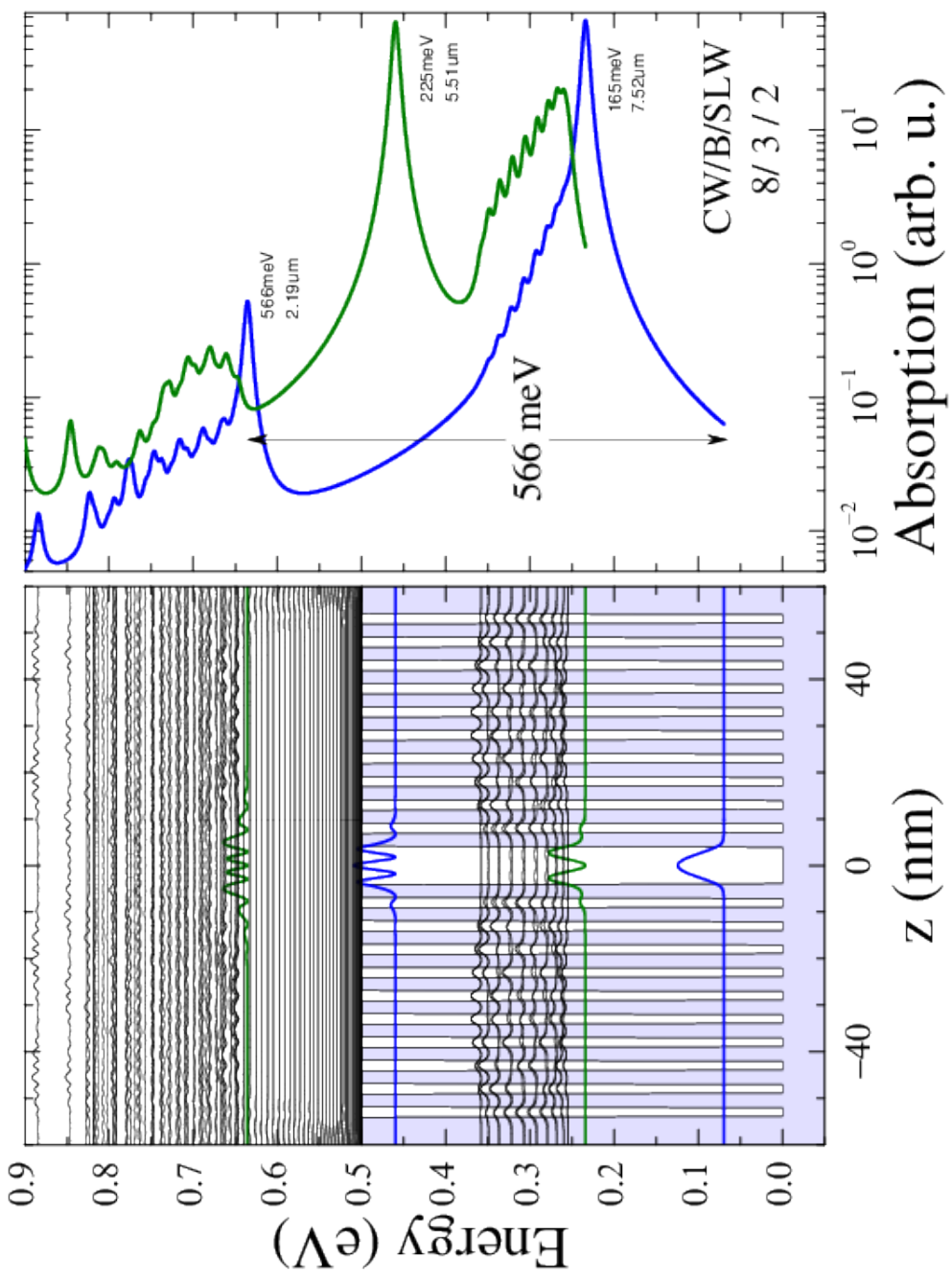

Figure 4.1: Sample NR0206. Theoretical simulation for central well 8 nm, barrier 3 nm and lateral well 2 nm. On the left side the sample structure and the probability density for the differents states is shown. On the right side the absorption obtained from the simulation is plot, the blue curve represent transitions from the ground state and the green curve transitions from the first excited state.

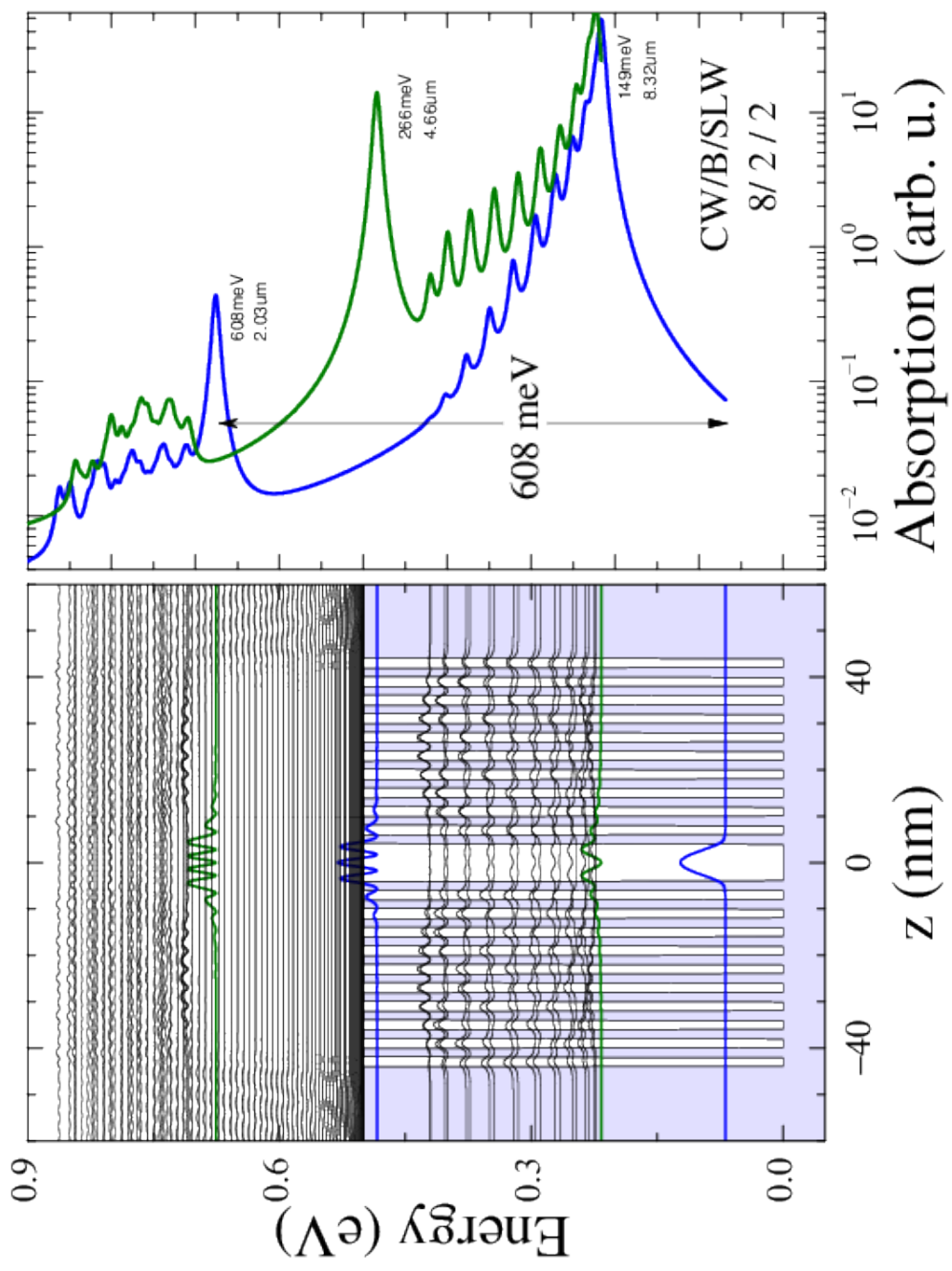

Figure 4.2: Sample NR0205. Theoretical simulation for central well 8 nm, barrier 2 nm and lateral well 2 nm. On the left side the sample structure and the probability density for the differents states is shown. On the right side the absorption obtained from the simulation is plot, the blue curve represent transitions from the ground state and the green curve transitions from the first excited state.

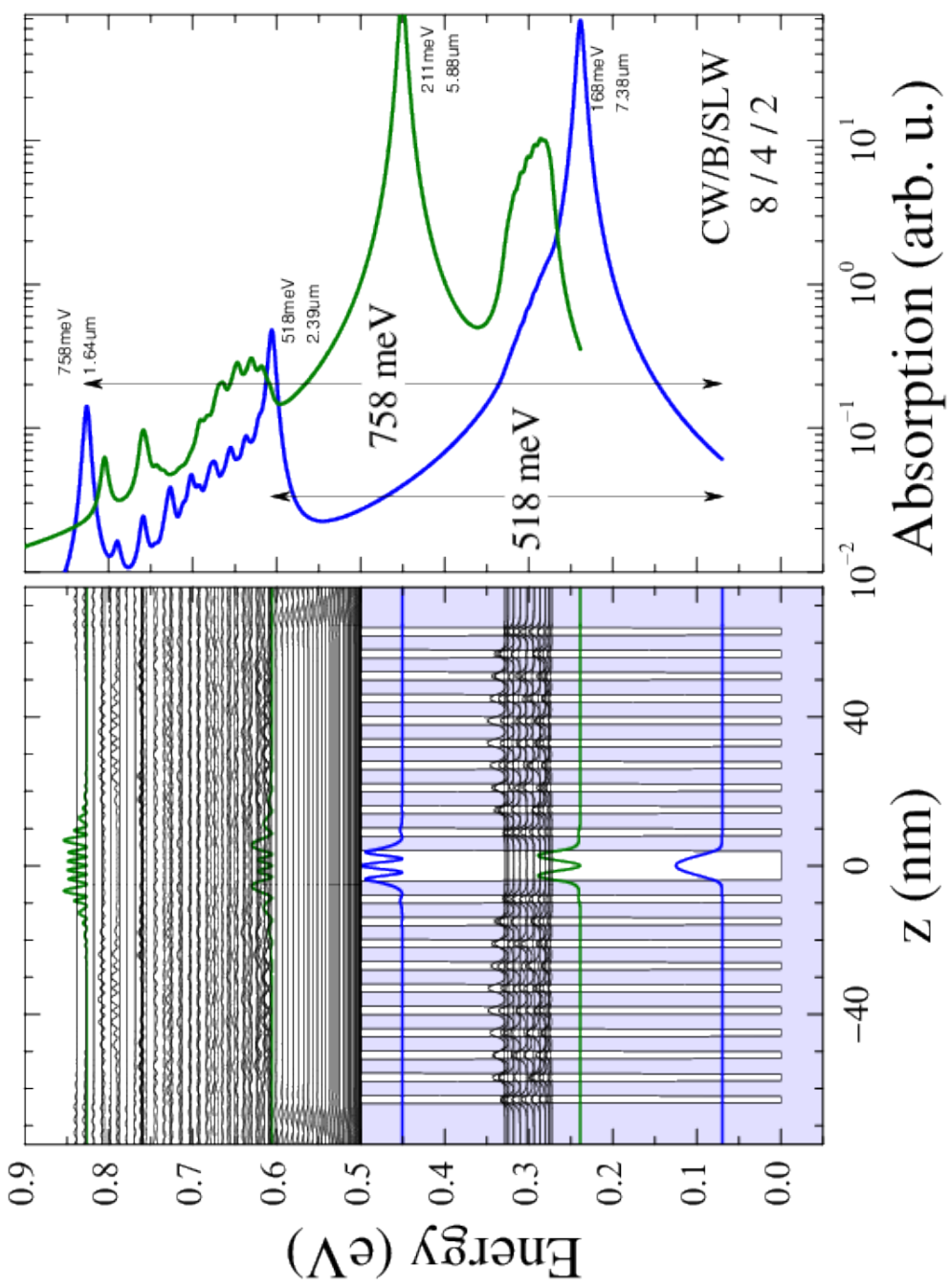

Figure 4.3: Sample NR0207. Theoretical simulation for central well 8 nm, barrier 4 nm and lateral well 2 nm. On the left side the sample structure and the probability density for the differents states is shown. On the right side the absorption obtained from the simulation is plot, the blue curve represent transitions from the ground state and the green curve transitions from the first excited state.

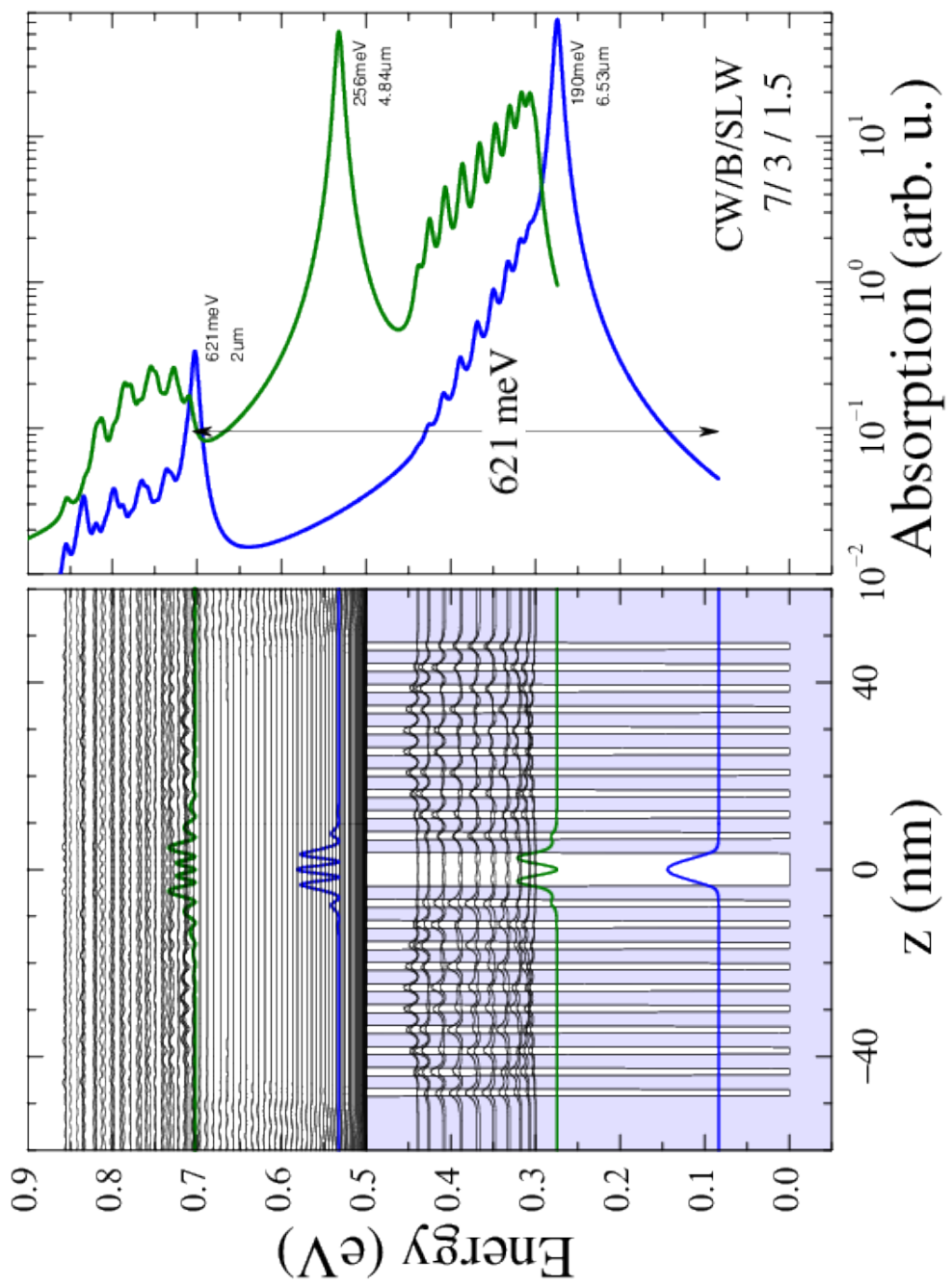

Figure 4.4: Sample NR0203. Theoretical simulation for central well 7 nm, barrier 3 nm and lateral well 1.5 nm. On the left side the sample structure and the probability density for the differents states is shown. On the right side the absorption obtained from the simulation is plot, the blue curve represent transitions from the ground state and the green curve transitions from the first excited state.

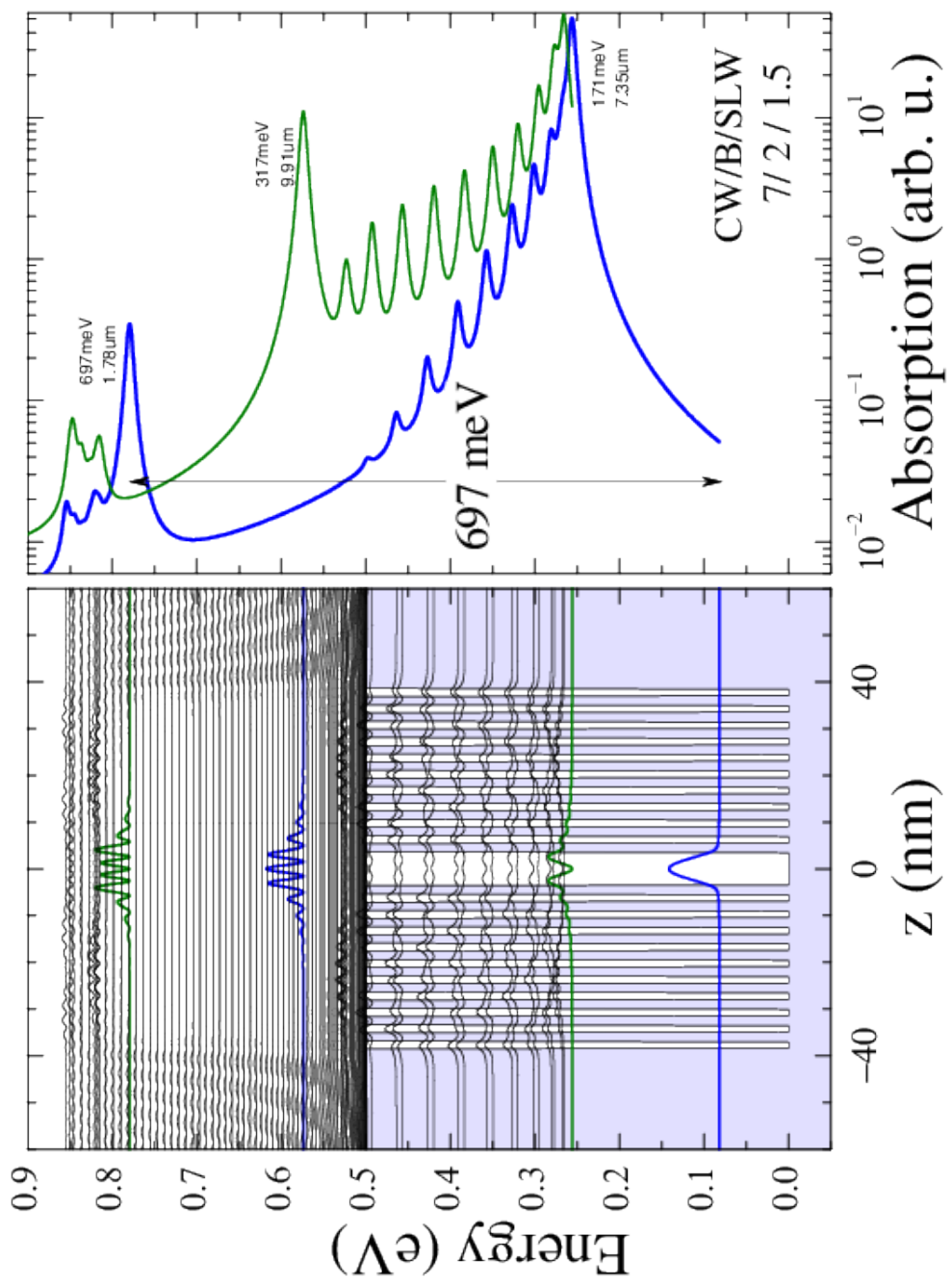

Figure 4.5: Sample NR0202. Theoretical simulation for central well 7 nm, barrier 2 nm and lateral well 1.5 nm. On the left side the sample structure and the probability density for the differents states is shown. On the right side the absorption obtained from the simulation is plot, the blue curve represent transitions from the ground state and the green curve transitions from the first excited state.

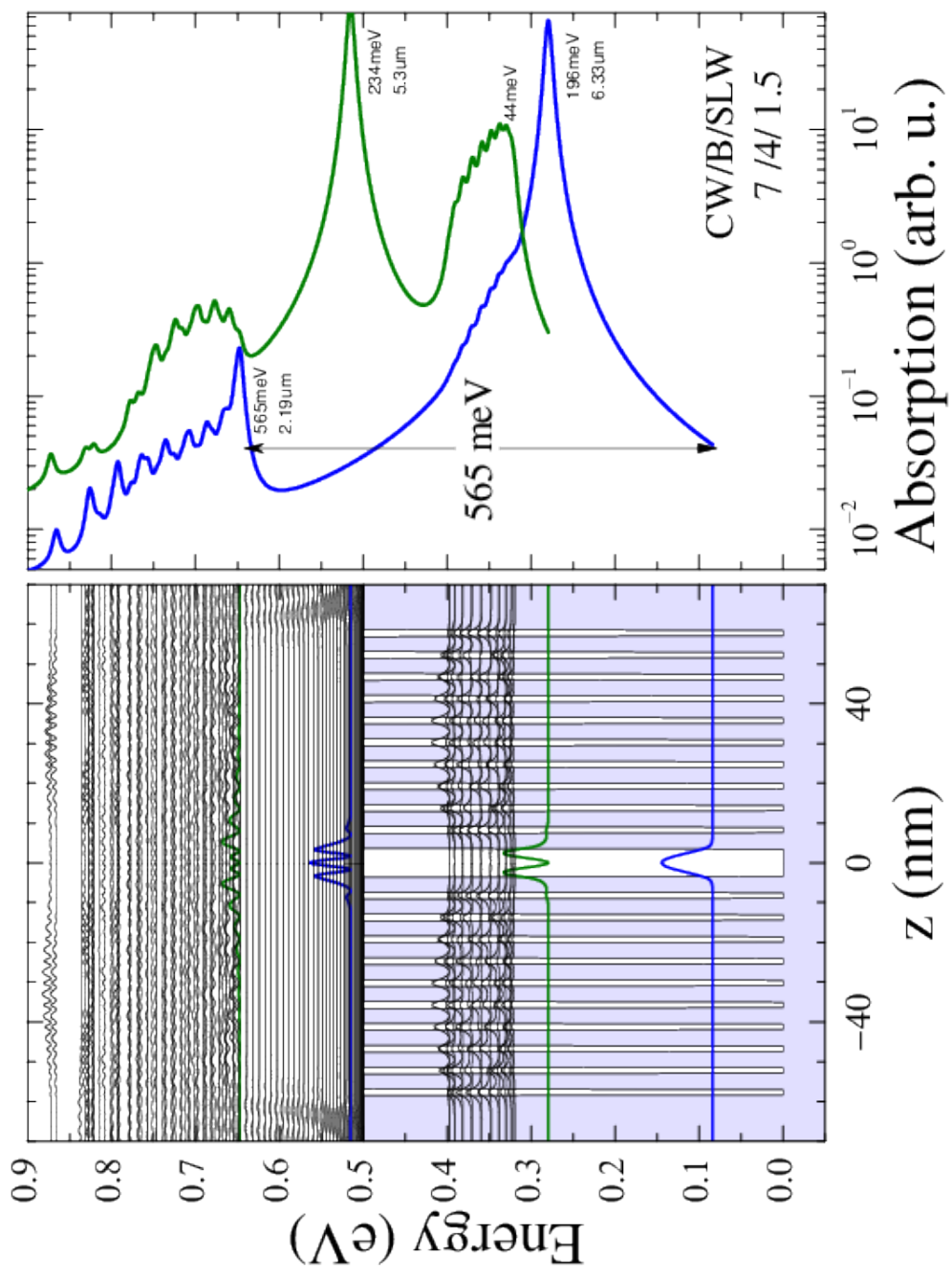

Figure 4.6: Sample NR0204. Theoretical simulation for central well 7 nm, barrier 4 nm and lateral well 1.5 nm. On the left side the sample structure and the probability density for the differents states is shown. On the right side the absorption obtained from the simulation is plot, the blue curve represent transitions from the ground state and the green curve transitions from the first excited state.

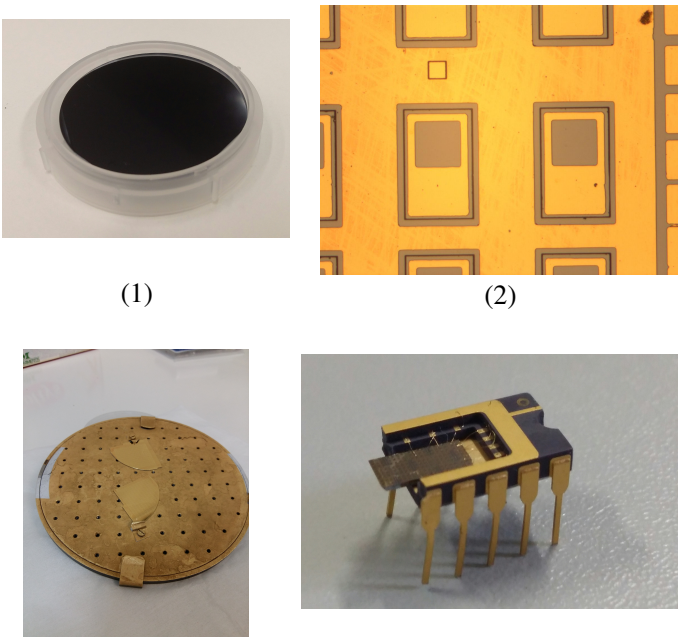

(1) (2)

(3) (4)

Figure 4.7: Samples production

Thus, the samples to be grown are: first three samples with a CQW thickness of 8 nm, LQW of 2 nm and barriers of 2 nm (sample NR0205), 3 nm (sample NR0206) and 4 nm (sample NR0207). Then other three samples with a CQW thickness of 7 nm, LQW of 1.5 nm and barriers of 2 nm (sample NR0202), 3 nm (sample NR0203), and 4 nm (sample NR0204).

4.2 Production of the QWIPs

After growth (figure 4.7-1), the samples are processed as explained in the previous chapter. The first lithography allows us to make the pattern of the mesas for the corrosion, and the second the pattern for the metalization. Figure 4.7-2 presents the sample after the second lithography; at this point the samples are ready to be metalized (figure 4.7-3). All these procedures, for the first set of samples, were performed at LabSem of the PUC-RIO and, for the second set of samples (which will be discused later), at the laboratory of the University of Campinas (UNICAMP), Sao Paulo, Brazil. Once processed, the samples are mounted on a chip and contacts are made, this step was done at Brazilian Center for Physics Research (CBPF), Rio de Janeiro, Brazil. The samples are then ready to be characterized; the finished device is shown in figure 4.7-4.

4.3
First set of samples

4.3.1
Absorption

The first measurement to be performed is the absorption. As explained in the previous chapter, we use the FTIR to obtain the absorption spectra of the samples applying radiation. Figure 4.8 shows the samples absorption spectra obtained. We observe in all of them a strong absorption peak between 150-185 meV, this peak corresponds to an absorption due to the transition between the ground state and the first excited state, for which the oscillator strength is the strongest.

These absorption peaks, that we see in figure 4.8, were predicted by the theoretical simulations (section 4.1). Figure 4.9 shows the energies of the absorption peaks obtained in the measurement and the one obtained by the simulations for each sample, we can see that the results are consistent with theoretical expectations. The peaks obtained in the simulations are of an energy slightly higher than those obtained experimentally, this difference may be due to a small variation in the thickness of the layers during growth.

From the absorption curves (figure 4.8) we measure the full width at half maximum (FWHM) $\Delta\lambda$, of each peak λ and we calculate $\Delta\lambda/\lambda$ for the peaks of the samples,

Sample	Absorption peak (meV)	$\Delta\lambda/\lambda$
NR0202	155	11%
NR0203	172	10%
NR0204	184	9%
NR0205	146	13%
NR0206	152	14%
NR0207	159	12%

As we can see all the samples have an absorption peak, corresponding to a transition from the ground state to the first excited state, with a $\Delta\lambda/\lambda$ between $9\% - 14\%$; to compare, a $\Delta\lambda/\lambda$ around 30% corresponds to transitions to the continuum and around 10% to transitions between bound states [25], demonstrating that the transitions are bound to bound. The fact that some peaks are wider may be related to the proximity to the miniband.

These peaks are not the ones we are most interested in, we expect to obtain a higher absorption energy from the transitions between the ground state and the third excited state. However, according to the theory, they have an oscillator

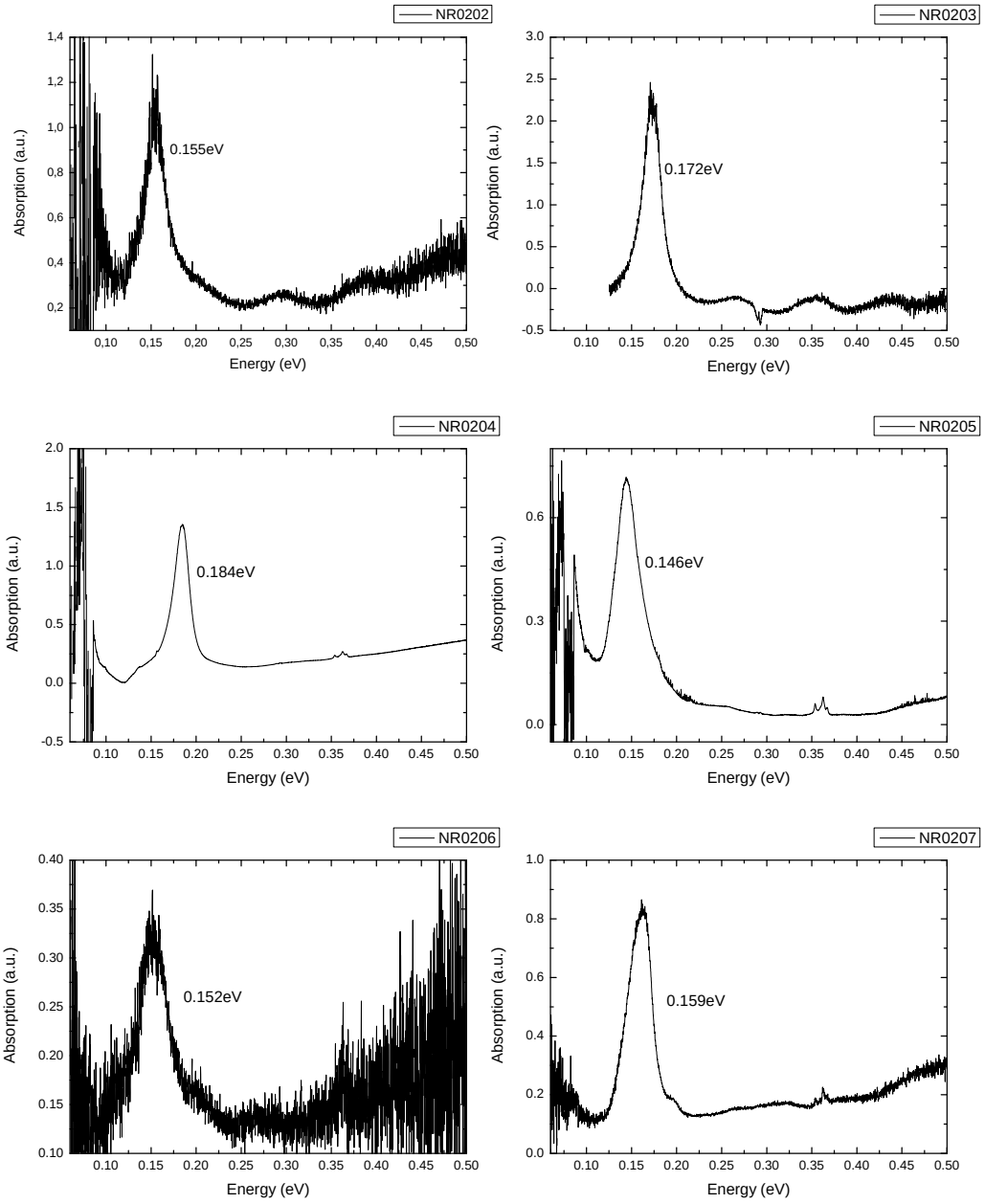

Figure 4.8: Absorption measurement for different samples, the peak observed comes from transitions between the ground state and the first excited state, which has the strongest oscillator strength.

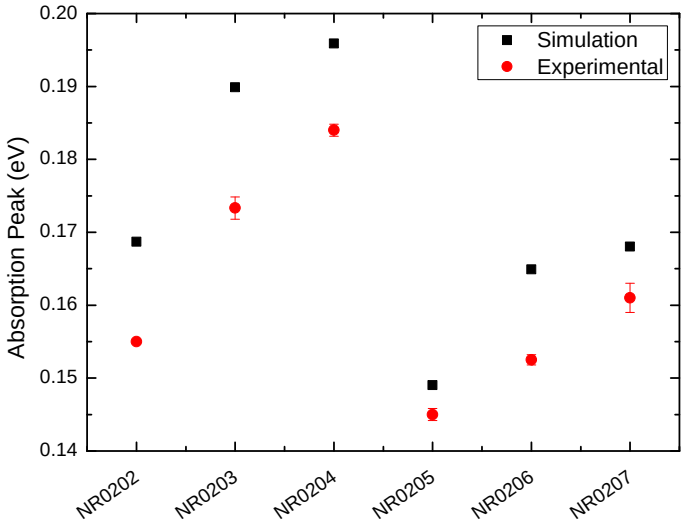

Figure 4.9: Expected absorption energies from theoretical simulations for transitions between ground state and first excited state and experimentally measured absorption

strength much lower than the main peaks, as we also saw in the simulations, as consequence it was not possible to detect them in absorption.

4.3.2 Dark current and photocurrent

Before measuring the photocurrent of the devices we measure the dark current, as explained in the previous chapter. The dark current limits the performance of the devices and that is why this is a very important measurement to be carried out.

The dark current measurements were made in LabSem at PUC-RIO as explained in the previous chapter. Figure 4.10 shows the IV curves obtained for the devices. We can see that the IV curves are not symmetrical with respect to the applied voltage, this may be due to the non-uniform distribution of the carriers or to the non-symmetric distribution of the InGaAs/InAlAs interfaces during growth [25, 26, 27].

When we analyse the IV curves we see that the dark current is very high. Even when lowering the temperature to 30K we do not manage to obtain a current lower than $\sim 10^{-3}$A, except for sample NR0204. With such high dark current it is difficult to detect a photocurrent.

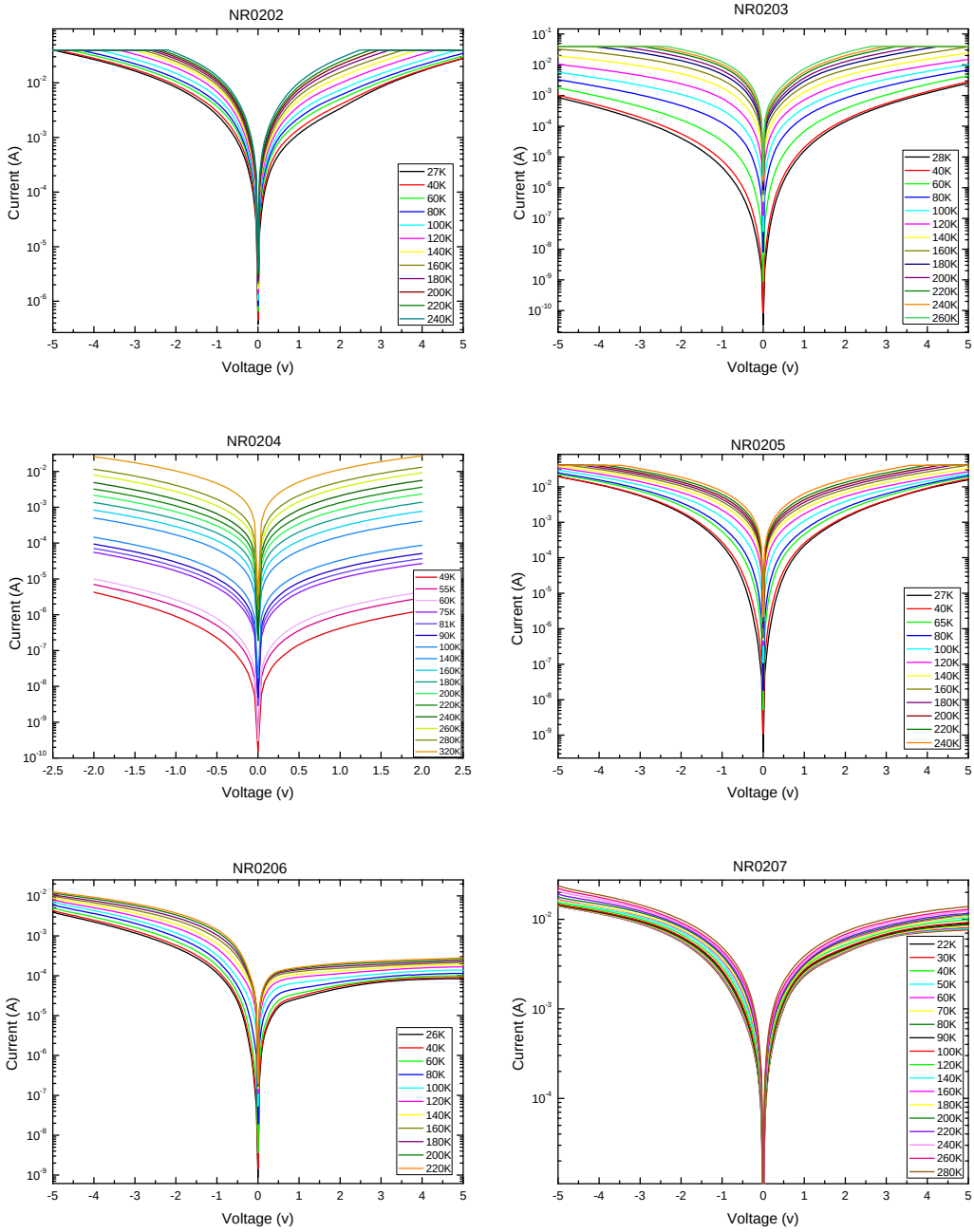

Figure 4.10: IV measurements showing dark current for different samples.

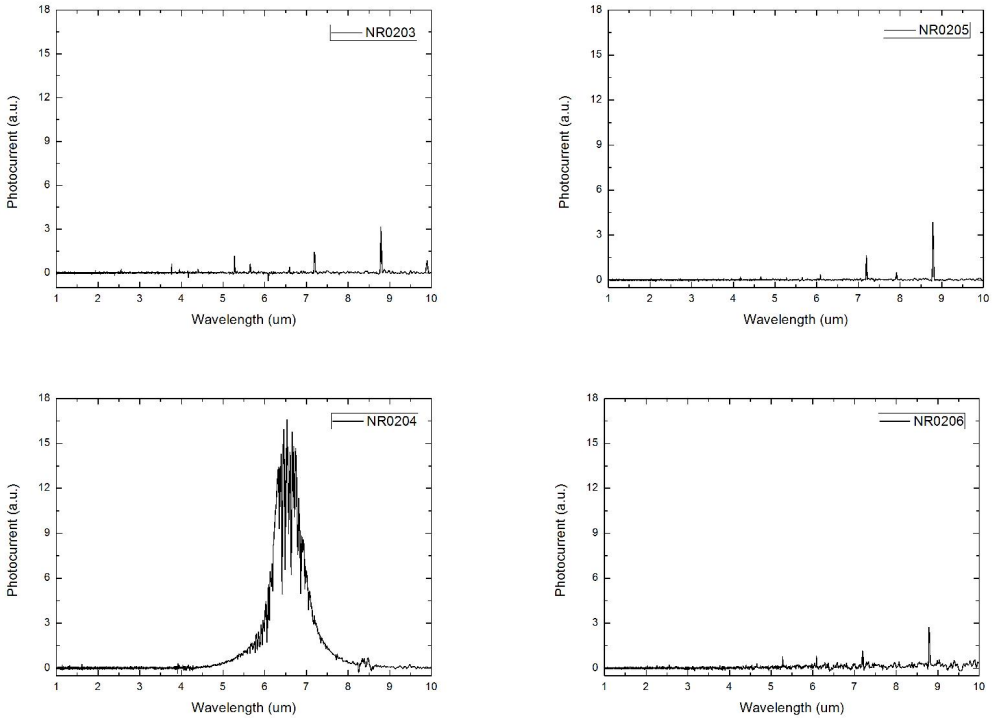

Figure 4.11: Photocurrent measurements, due to high dark current it was not possible to measure photocurrent.

Nevertheless, we have measured the photocurrent for these samples with the procedure explained in the previous chapter, the obtained results are shown in figure 4.11. As we can see it was not possible to obtain the desired photocurrent, even at lower temperatures.

For the samples NR0202 and NR0207 it was not possible to measure photocurrent due to the fact that the noise was too high for the equipment to respond.

For samples NR0203, NR0205 and NR0206 even though the equipment allowed the photocurrent measurement, no signal was detected. Sample NR204, which was the one that had lower dark current (although not as low as we desired), presents a photocurrent peak at 189 meV. This peak is consistent with the one obtained in the absorption (184 meV) and it comes from a transition between ground state and the first excited state. In principle this absorption should not generate photocurrent, since after the transition the electron is still inside the well. However, as we see in the theoretical simulations (figure 4.6), the sample has a miniband just above the first excited state. When we apply bias, this miniband tilts and the state overlap with the miniband then, after the transition from the ground state to the first excited state, the electron could generate photocurrent through this miniband. Since the spacer

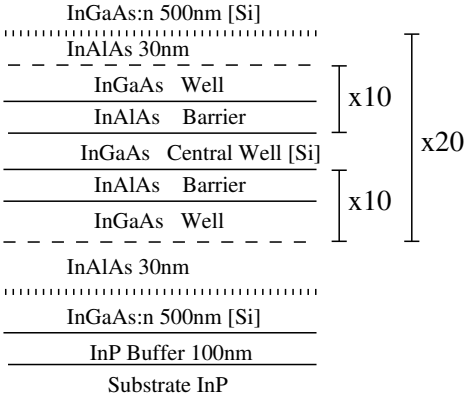

Figure 4.12: Sample structure for the second set of sample. The spacing between the neighboring superlattice was increased to 30 nm.

between each superlattice is only 10 nm, electrons tunnel through the entire structure producing the photocurrent. This indicates that this spacer is not thick enough to avoid the dark current, as well. Therefore we decided to grow another 2 new samples with wider spacing between neighboring superlattices.

4.4 Second set of samples

The structure of the new samples grown are shown in figure 4.12, the spacing between the neighboring superlattices was changed from 10 nm to 30 nm, in order to prevent tunneling between them, thereby reducing the dark current. The samples grown are: NR0419 (equivalent to NR0203) with a CW of 7 nm, LW of 1.5 nm and barriers of 3 nm, and NR0421 (equivalent to NR0205) with a CW of 8 nm, LW of 2 nm and barriers of 3 nm, both with a doping of $1.56 \cdot 10^{18} cm^{-3}$. These samples were chosen because they are those that showed best result from the previous set of structures. The calculated brandstructure at 0 K together with the different probability densities for the structures is depicted on the left side of Fig. 4.13, superimposed on the conduction band profile for the structure in null bias.

Continuing with the same notation used in the graphics of the previous structures, in blue are the probability densities for states localized in the CQW with even parity, while in green are the ones for odd parity. On the right of the same figure, the calculated absorption spectra are shown. As in the previous structures, the blue line denotes absorption from the ground state and the green line from the first excited state. As explained previously, only transitions involving a change in parity between initial and final states are allowed by the electric dipole selection rule. Also, only transitions from the ground states are expected, transitions from the first excited states should not

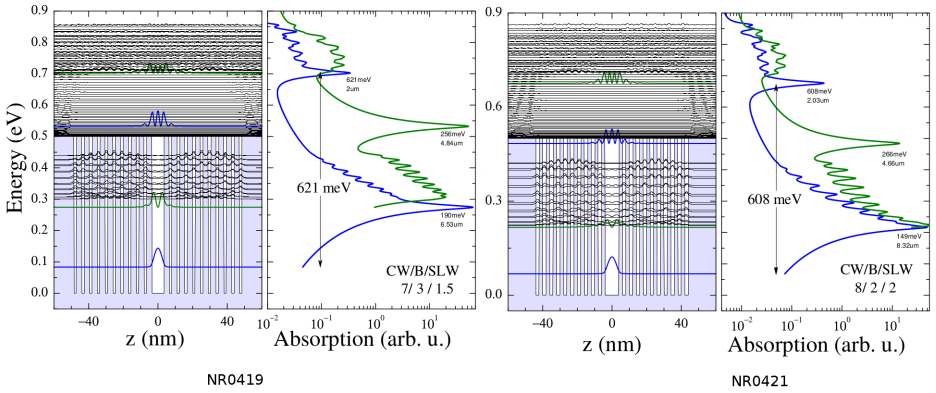

Figure 4.13: Sample NR0419 and NR0421. Theoretical simulation for central well 7 nm, barrier 3 nm and lateral well 1.5 nm (NR0419) and central well 8 nm, barrier 2 nm and lateral well 2 nm (NR0421). On the left side the sample structure and the probability density for the differents states is shown. On the right side the absorption obtained from the simulation is plot, the blue curve represent transitions from the ground state and the green curve transitions from the first excited state.

generate any absorption because the doping level used it should not be enough to populate this energy level.

With these theoretical results we expect two absorption peaks, the strongest at 190 meV for sample NR0419 (at 149 meV for sample NR0421) and the second one, about two order of magnitude weaker, at 621 meV for NR0419 (at 608 meV for NR0421). Additionally, a series of peaks are observed in the ranges between 200 and 300 meV and between 600 and 750 meV, which refer to transitions to the two different miniband states.

4.4.1 Absorption

As for the first set of samples we have measured the absorption spectra for p-polarized incident light at room temperatura of the new structures. The obtained results are shown in figure 4.14. We observe a strong peak at 188 meV for the sample NR0419 and one at 158 meV for NR0421, these results are consistent with expectations from theoretical simulations, 190 meV and 149 meV, respectively and are absorptions that come from transitions between the ground state and the first excited state. These absorption peaks should not generate photocurrent since the electrons after the absorption are still trapped in the quantum well. We obtain a $\Delta\lambda/\lambda$ of 11% and 13% for the samples NR0419 and NR0421, respectively, whereby the absorption comes from a bound to bound transition.

No peak is observed around 206 meV, indicating that, as expected, the first

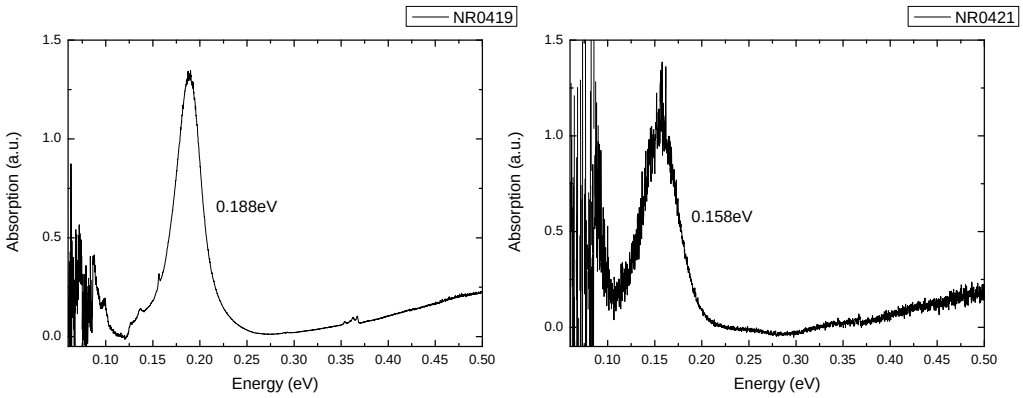

Figure 4.14: Absorption measurement showing the absorption from the transition between the ground state and the first excited state, which have the strongest oscillator strength.

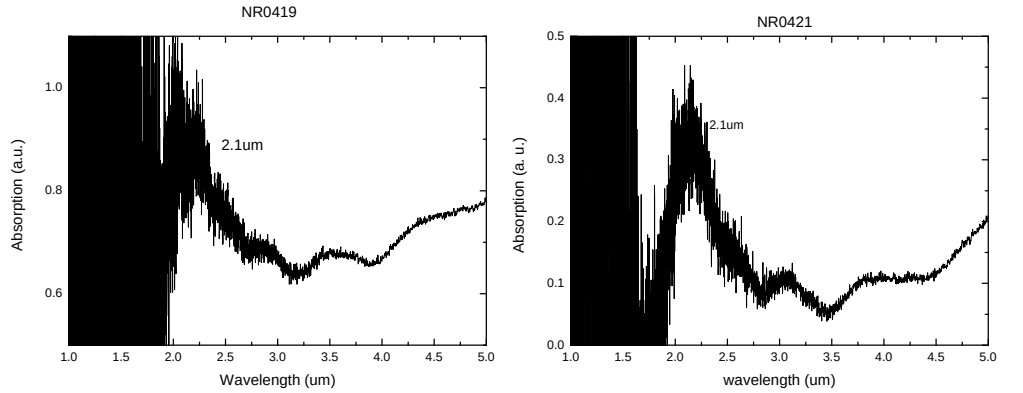

Figure 4.15: Absorption measurement showing the absorption from the transition between the ground state and the third excited state.

excited state is not populated and therefore, does not give rise to an absorption signal.

The absorption in the region of interest, at higher energies, is shown in figure 4.15. In spite of being in the limit recommended for the detector used in this measurement, we can observe an absorption peak at $\sim$2.1 μm in both samples ($\sim$590 meV) about 90 meV above the bandoffset, these peaks are consistent with the expected values from the simulations.

A red shift in the experimental data compared to the calculated energy is observed, which is due to the structure real dimensions departing from the nominal values. In order to exhibit this, we slightly changed the dimensions of the structure NR0419 to a CQW of 7.1 nm, barriers of 3.2 nm and SLW of 1.8 nm, to best fit the experimental results, the calculated absorption spectra for this new thicknesses for sample NR0419 are shown in figure 4.16. Similar

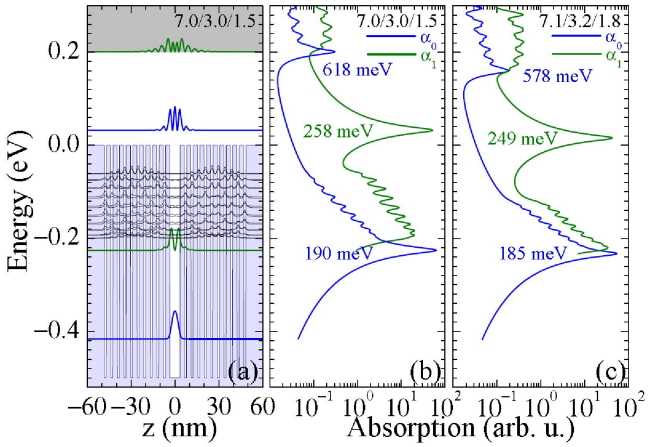

Figure 4.16: (a) probability densities for the first four localized states (blue for even and green for odd parity states) and for the miniband states (grey) superimposed on the conduction band profile on the growth direction. (b) absorption spectra for transitions with the ground state (blue) and the first excited state (green) as the initial states for the nominal structure thicknesses. (c) absorption spectra for transitions with the ground state (blue) and the first excited state (green) as the initial states for the best fit structure thicknesses.

changes were perfomed for sample NR0421 and the values for the best fit absorption spectrum were CW of 8.2 nm, barriers of 3.2 and a SLW of 2.4 nm.

4.4.2 Dark current

After processing the samples and fabricate the devices we measure the dark current of the new structures, figure 4.17, we see that the dark current is much lower than the one measured in the previous set of devices, achieving a current as low as $10^{-10}A$ at lower temperatures (77K). This shows that if we have superlattices too near to each other, we have tunnelling between them and, thereby we have an increase of the dark current.

With the data from the IV curves, we graph the Arrhenius plot (top figure 4.18 and 4.19) where we can see the logarithm of the current as a function of 1/kT and observe that at high temperatures the curve has a tendency to a straight line. Considering the inclination of the curves at high temperatures we determine the activation energy for different applied bias, also shown in figure 4.18 and 4.19 (bottom).

In both samples we see that when we increase the applied voltage the activation energy decreases, this result is associated with the thermally assisted tunnelling because with higher applied voltage tunnelling becomes easier.

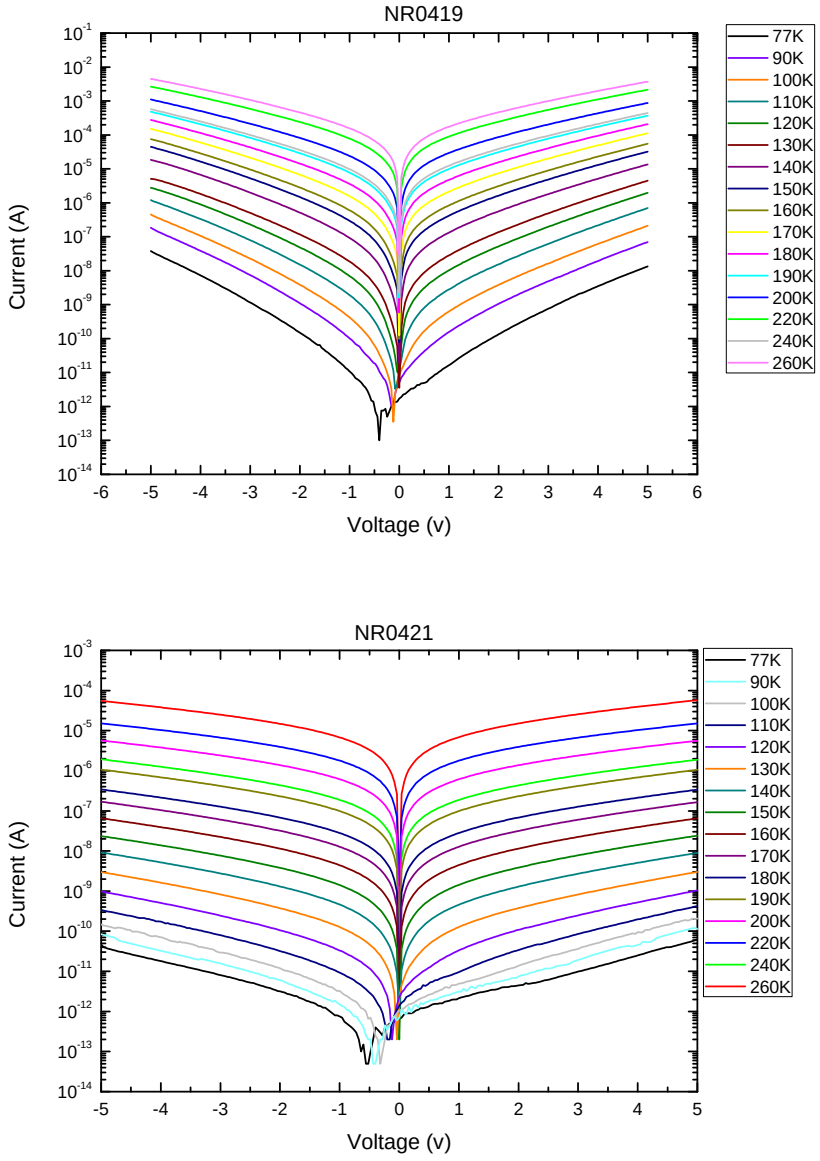

Figure 4.17: Dark current as function of the temperature of the samples NR0419 and NR0421.

The activation energy for 0 bias is 267 meV for sample NR0419 and 170 meV for NR0421, which is consistent with the energy difference between the Fermi level (77 meV above the ground level) and the extended states of the first miniband, according with the calculations. This result can be explained by the thermally assisted tunneling mechanism, where electrons are thermally activated from the ground state to the miniband and then they tunnel from one SL to the adjacent one through the 30 nm InAlAs spacer. With a smaller spacer this effect would be much higher, that is why is important to have a spacer bigger enough to reduce this tunneling.

4.4.3 Photocurrent

In order to measure the current generated by our photodetectors we perform the photocurrent measurement as explained in the previous chapter. The results obtained for the sample NR0419 are shown in figure 4.20 and 4.21, the photocurrent was measured at 77K and with different bias applied.

A main photocurrent peak is observed at 587 meV (2.11 μm), this peak comes from a transition between the ground state and the third excited state, in accordance with the peak obtained in the absorption measurement and in agreement with the one predicted by the theoretical simulation. When we apply different voltages this peak does not shift, it remains with the same energy, as was also predicted by the theoretical simulations and will discussed below.

We also observe a second peak at 276 meV (4.5 μm), this peak is wider because it does not comes from a transition bound to bound as the main peak, it comes from a transition between the ground state and the miniband inside the quantum well. As we see in the simulations (figure 4.4) there is a miniband inside the well just above the second excited state, the peak observed in the photocurrent around 0.3 meV coincides with a transition from the ground state to this miniband. The photocurrent is produced by applying bias and the electrons leave the quantum well by tunnelling. This peak shows in the middle a dip in the photocurrent due to the absorption of CO_2 and will be present in all the photocurrent measurement since no CO_2 purge was performed on these experiments.

There is a second possibility that would explain this peak in the photocurrent. If the first excited state were populated (it should not be by design), a transition from this state to the second excited state could generate an absorption at ~ 0.3 meV that would also explain the peak in the photocurrent.

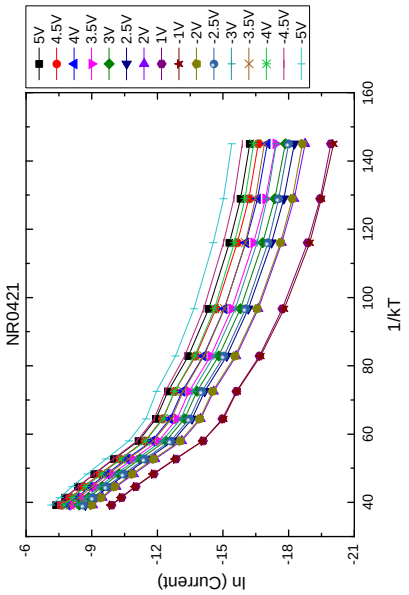

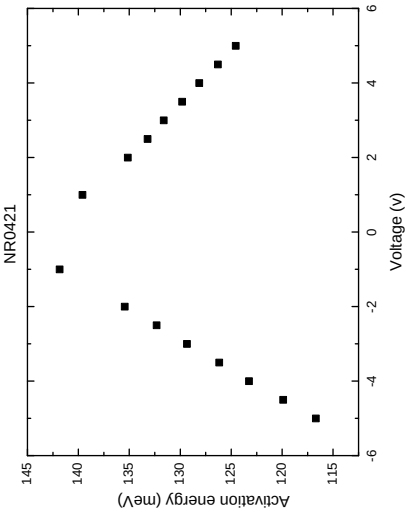

Figure 4.19: Arrhenius curve and Activation energy as function of bias for sample NR0421.

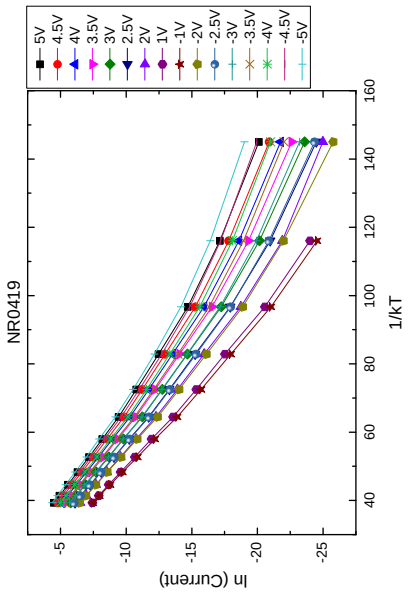

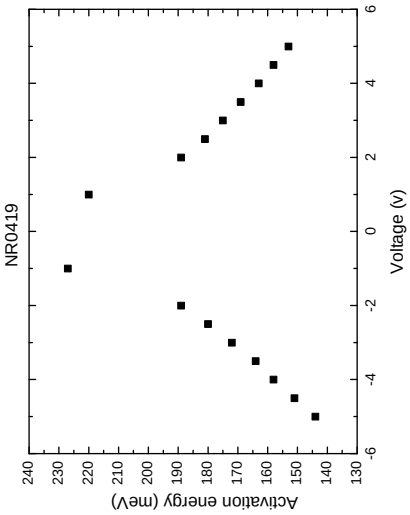

Figure 4.18: Arrhenius curve and Activation energy as function of bias for sample NR0419.

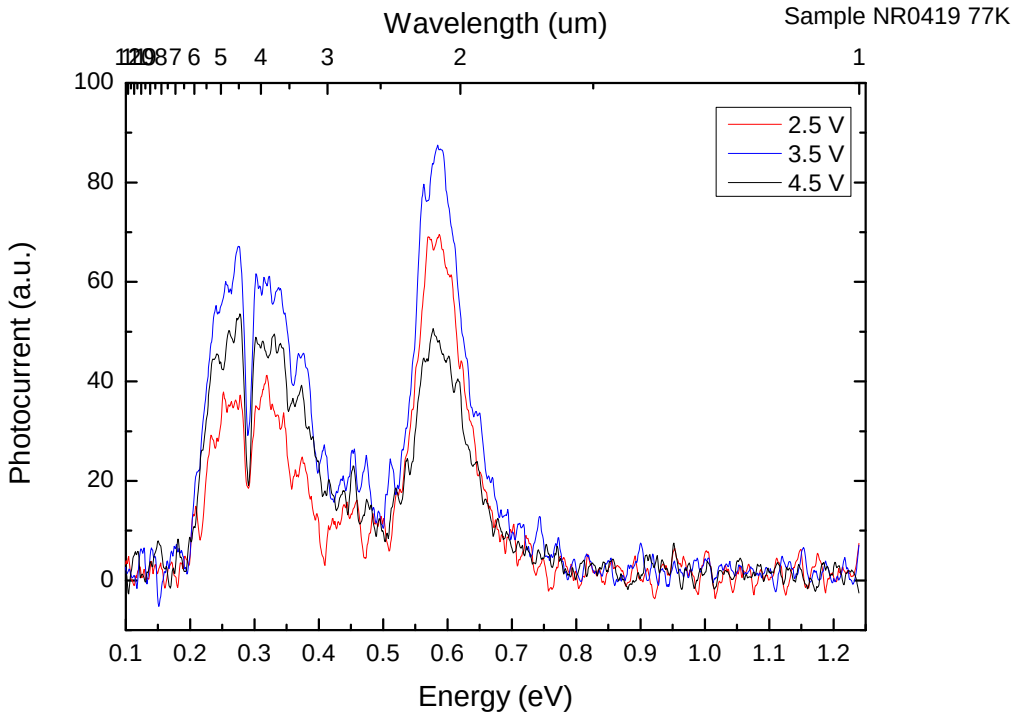

Figure 4.20: Photocurrent of sample NR0419. Bias: 2.5V, 3.5V and 4.5V

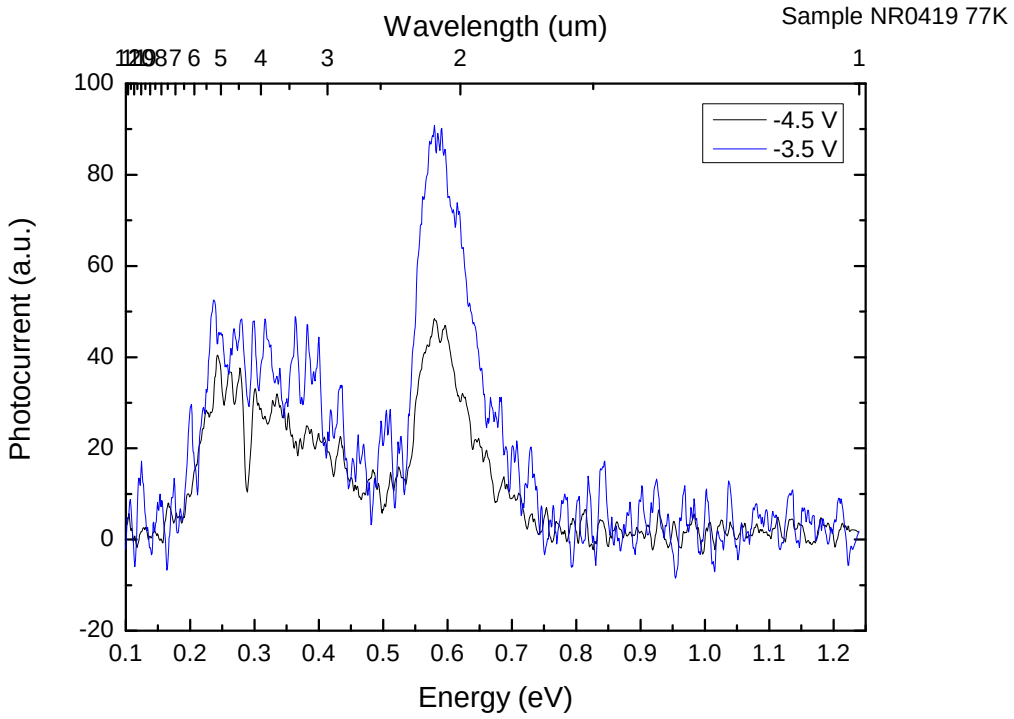

Figure 4.21: Photocurrent of sample NR0419. Bias: -4.5V and -3.5V

In order to elucidate the origin of this peak, simulations at different bias were performed. Figure 4.22-a shows the absorption at different electric fields. From the bottom to the top, the curves represent the absorption with the electric field from 0 to 29 kV/cm (equivalent to 7.5 V applied bias) for transitions from the ground state (blue curve in figure 4.4) and figure 4.22-b for transitions from the first excited state (green curve in figure 4.4). The zero of energy in these plots represent the energy of the initial state of the transition, the ground state for 4.22-a and the first excited state for 4.22-b.

We observe that the absorption peaks that come from the transition from the ground state to the third excited state and to the miniband do not shift when we apply different bias, in agreement with the experimental results. The same occurs for transitions from the first excited state to the miniband. However, absorptions coming from transitions from the first excited state to the continuum disappear with increasing electric field. In the experimental results we do not obtain any peak that disappears with bias, then, we do not have any absorption coming from transitions from the first excited state.

Consequently, the peaks of photocurrent that we have obtained experimentally are in fact due to transitions from the ground state to the third excited state and to the miniband that was created in the quantum well.

The fact that the doping level is too low to populate the first excited level, as mentioned before, is an additional evidence that the transition should be the one from the ground state to the miniband. Once in the miniband where the states are more extended, the electrons may move to the borders of the SL and then tunnel through the InAlAs barriers, just as the thermally excited ones do to generate the dark current.

In figure 4.23 we present the photocurrent spectra obtained for the sample NR0421 applying positive voltage and in figure 4.24 applying negative voltage. This sample presents a main photocurrent peak at 523 meV (2.37 μm) that also does not shift when we applied different bias, in good agreement with the theoretical simulations. This peak comes from a transition between the ground state and the third excited states as we measured in the absorption.

As it was obtained for sample NR0419, here we again observe a second and wider peak around 0.2-0.3 meV that also could come from transitions between the ground state and the miniband or between the first excited state (if this state were populated) and the second excited state (figure 4.2).

In order to confirm to which transition this peak in the photocurrent corresponds simulations were also performed for different bias for this sample.

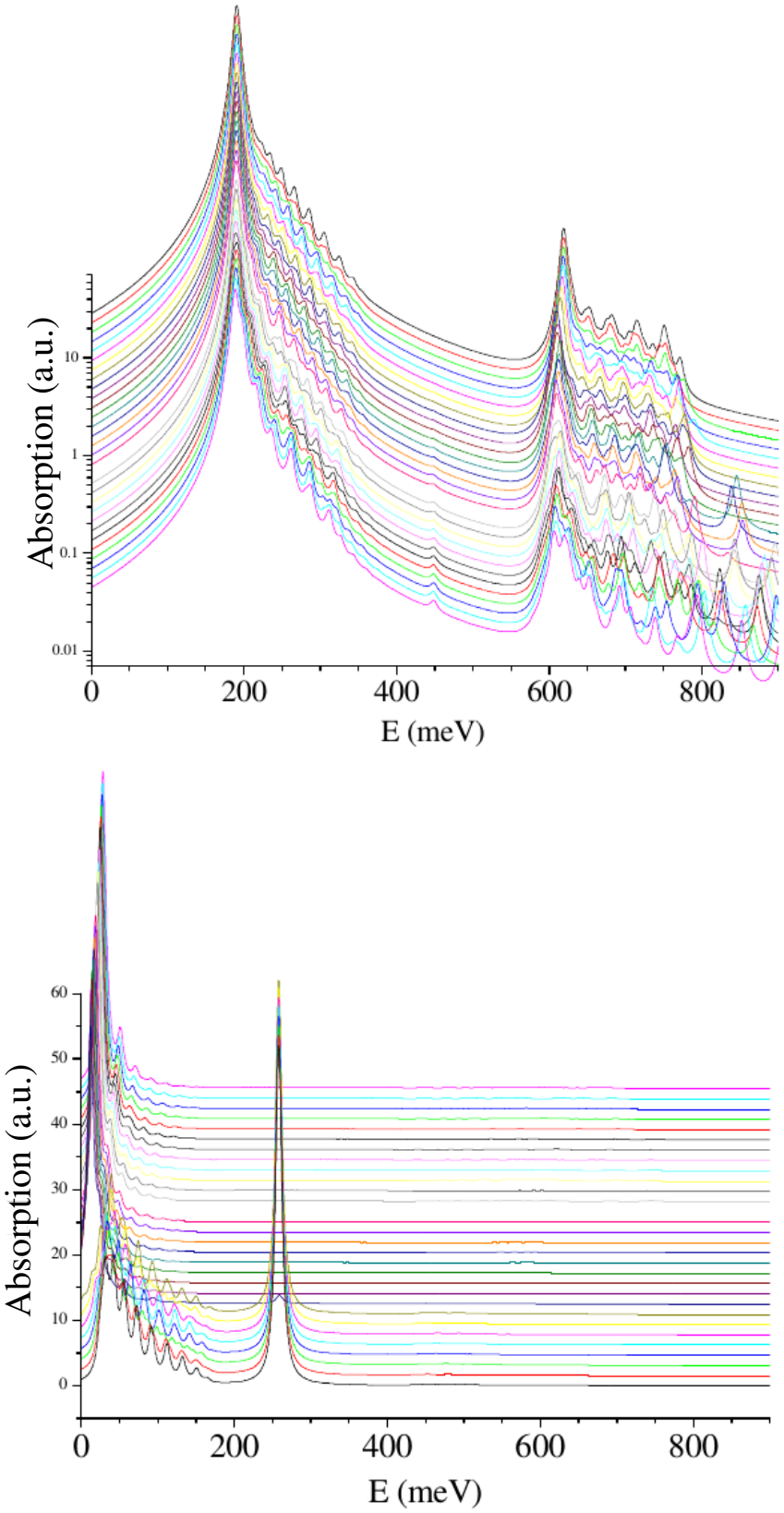

Figure 4.22: Theoretical simulations for different electric field applied on sample NR0419. From bottom to the top, the curves represent the absorption with electric field from 0 to 29 kV/cm (bias from 0 V to 7.5 V). Above: absorption obtained from transitions from the ground state, the zero of the energy axis represent the energy of this state. Bottom: absorption from transitions from the first excited state, the zero of the energy axis represent the energy of this state.

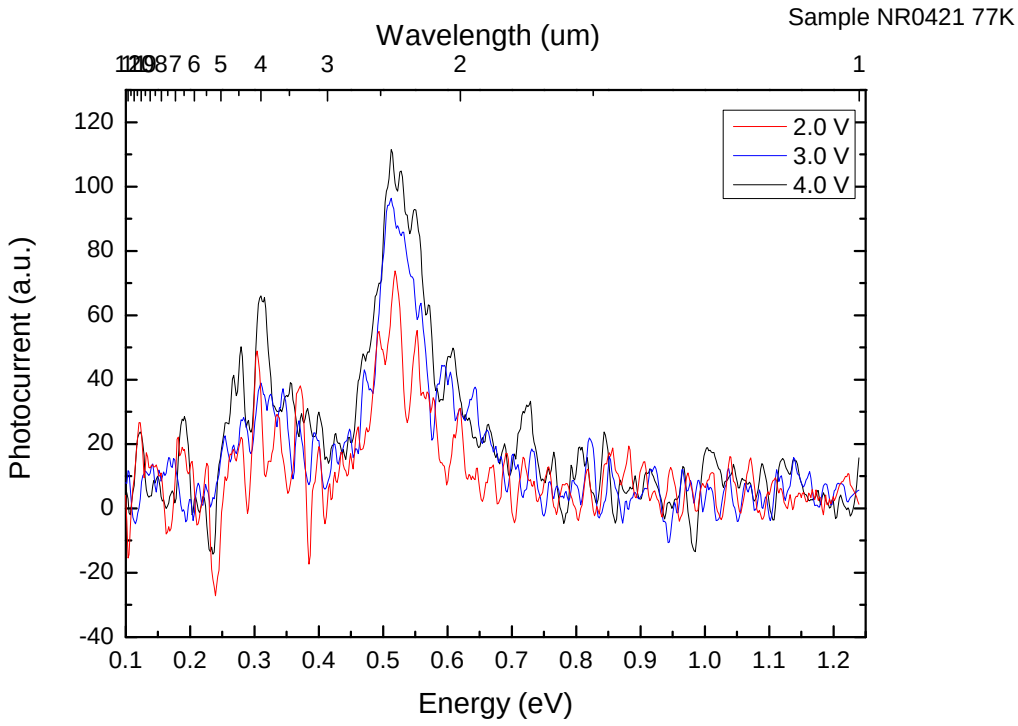

Figure 4.23: Photocurrent Sample NR0421. Bias: 2V, 3V and 4V

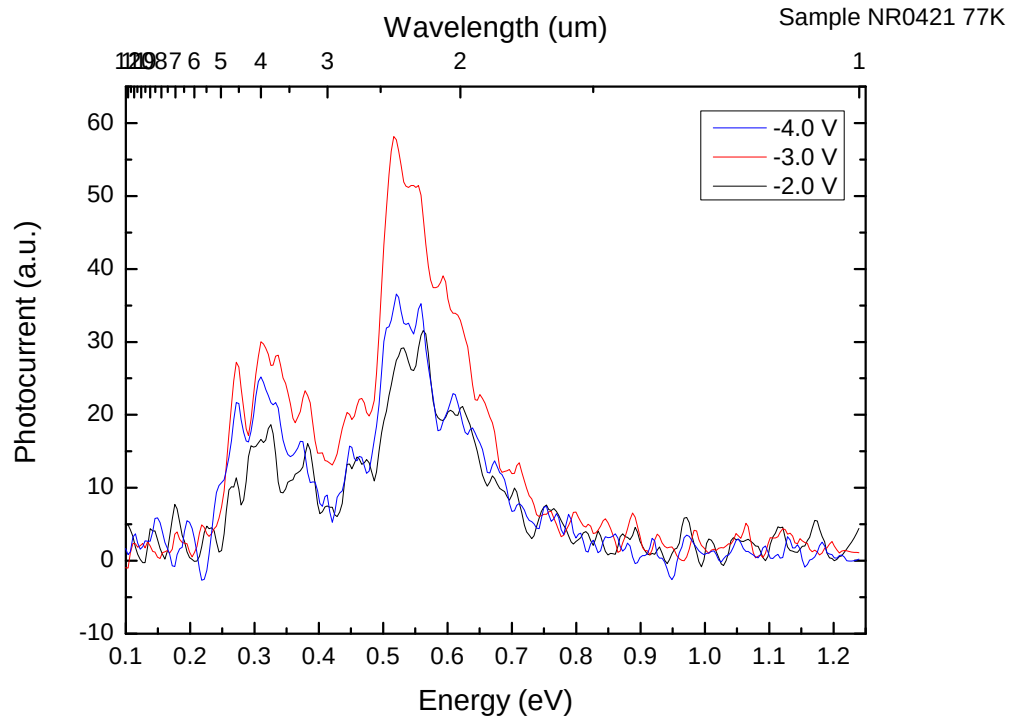

Figure 4.24: Photocurrent Sample NR0419. Bias: -4V, -3V and -2V

Figure 4.25-a shows the absorption obtained, from the bottom to the top, the curves represent the absorption with the electric field from 0 to 29 kV/cm (equivalent to 6.8 V applied bias) for transitions from the ground state (blue curve in figure 4.2) and figure 4.25-b for transitions from the first excited state (green curve in figure 4.2).

As in the previous results, for sample NR0421 we also found that absorption peaks from the transition from the ground state remain at the same energy when applying an electric field and that absorption peaks from transitions from the first excited state disappear with increasing electric field.

As this sample does not present any peak that disappears when applying bias in the experimental results, we conclude that the peaks observed in the photocurrent experiment are due to transitions from the ground state to the third excited state and to the miniband formed inside the quantum well.

The transitions from the first excited state were not present in the measurement of any sample since this state, in fact, is not populated. The thermal energy is not enough to populate this excited level, as expected.

We also observe that no photocurrent peak is detected at 190 meV for sample NR0419 (or at 149 meV for NR021), where the strongest peak was revealed in the absorption measurement and the largest oscillator strength calculated, this is due, as we have discuss in the previous chapter, to that the final state of the absorption is the first localized excited state, which is below the barrier conduction band, keeping the electrons confined, and, therefore, unable to generate a current.

We have found that both samples show photocurrent peaks at higher energies than the bandoffset limit in accordance with theoretical simulations and with what was expected from the design of the samples, demonstrating that with this spacially designed S-QWIPs, it is indeed possible to detect radiation for energies larger than the materials bandoffset.

Comparing our results to those obtained by Leavitt and Little [17], since their reported optical transition occurs between the ground level and the first localized excited state in the continuum, the corresponding oscillator strength is larger, on the other hand, the operation wavelength is longer. In our devices, we lose in oscillator strength as the final state of the absorption is the second excited one in the continuum, but we obtain energies larger than the bandoffset, meaning shorter wavelengths and, reaching the “forbidden gap” mentioned in the introduction.

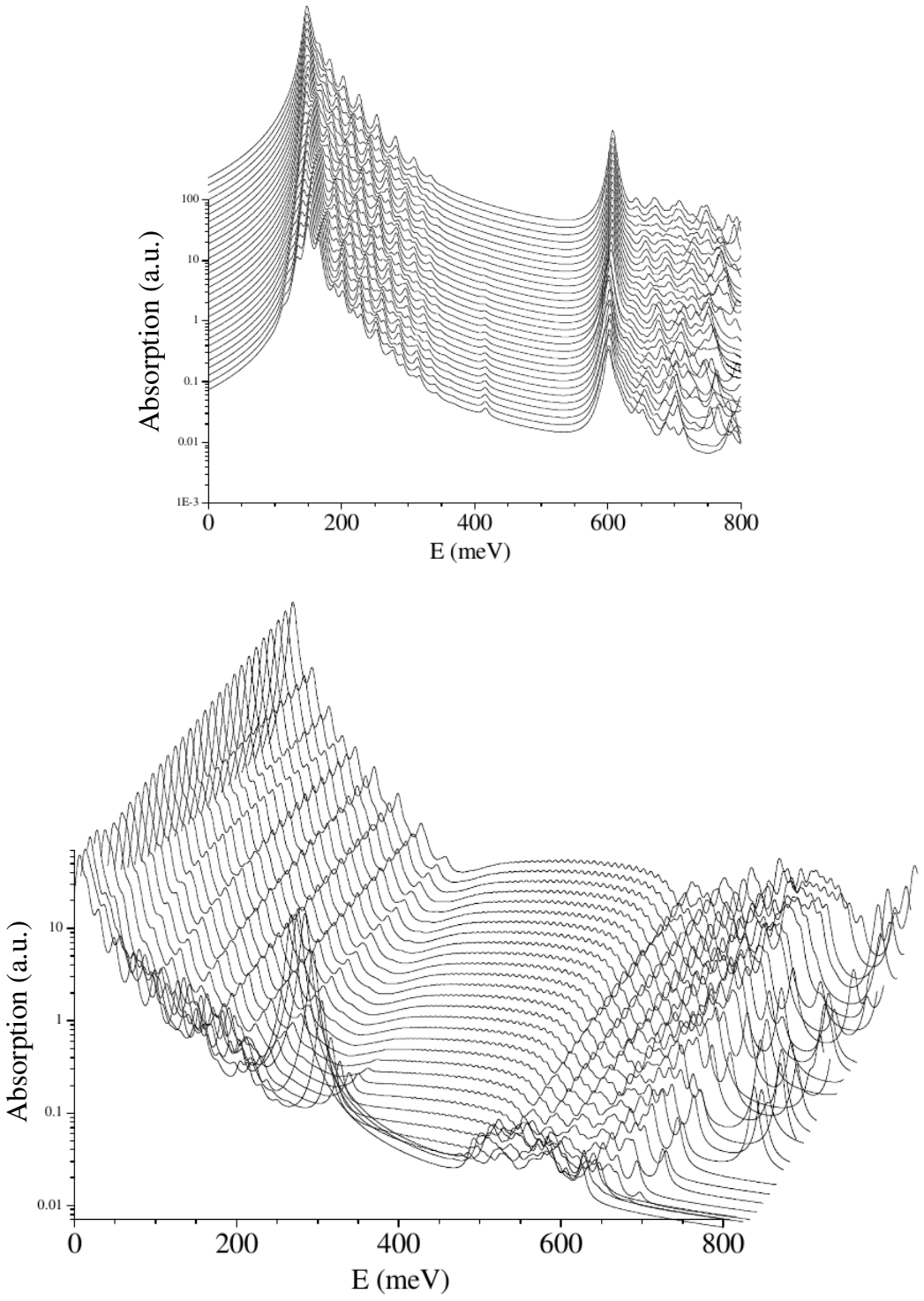

Figure 4.25: Theoretical simulations for different electric field applied on sample NR0421. From bottom to the top, the curves represent the absorption with electric field from 0 to 29 kV/cm (bias from 0 V to 6.8 V). Above: absorption obtained from transitions from the ground state, the zero of the energy axis represent the energy of this state. Bottom: absorption from transitions from the first excited state, the zero of the energy axis represent the energy of this state.

5
Conclusion and remarks

In this work InGaAs/InAlAs QWIP structures to detect radiation in the normally unreachable range with conventional intraband transitions in QWIPs based on III-V semiconductors, 1.7-3.1 μm, is proposed.

The theoretical approach used to understand the behaviour of the structures was explained. With the simulations we were able to design structures in the desired range of energy.

The InGaAs/InAlAs structures were grown by metalorganic vapor phase epitaxy lattice matched to the InP substrate, all the procedures that were performed in order to fabricate the photodetectors and all the experimental measurements that were carried out on the devices to test their performance were explained.

In the first set of samples we observed an absorption peak in agreement with what was theoretically expected, according to the simulations, but the IV measurement showed a high dark current that did not allow to measure a photocurrent. The high dark current was due to the tunneling through the neighboring superlattices due to the narrow spacer between them, so it was decided to grow another two samples with increased spacing between superlattices.

The second set of samples showed an absorption peak in accordance with what was expected by the simulations. The stronger peak was at 190 meV (6.6 μm) for the sample NR0419 and at 149 meV (7.8 μm) for the sample NR0421, these peaks coming from a transition from the ground state to the first excited state and did not show an equivalent peak in the photocurrent measurement, as expected, since after the transition the electrons are still trapped inside the quantum well and can not generate a current. The IV measurement showed a lower dark current than the previous samples did, confirming that the high dark current in the first set of samples was due to the tunneling through the superlattices and by increasing the spacing between them we managed to reduce it.

The photocurrent measurement showed a peak around 2 μm for both samples (587 meV for NR0419 and 523 meV for NR0421), consistent with the observed absorption peak, and in agreement with the one obtained from theoretical

simulations. The optical transition occurs between the ground state and the third excited state.

We also observed, in both samples, a wider peak in the photocurrent around 0.2 - 0.3 meV. Theoretical simulations were performed to confirm that this peak corresponds to a transition between the ground state and the miniband formed inside the quantum well. These results can also be confirmed by the fact that can not be a transition from the first excited state since this state was not populated.

Thus, in this work we fabricated QWIPs with which we managed to reach energies higher than the limit imposed by the bandoffset of the materials allowing to increase the detection range of the material. The measurements were performed at 77 K, for higher temperature operation two parameters are crucial for the design of S-QWIP structures, namely: the minibands should be energetically far from the energy levels involved in the absorption and the thickness of the spacer layer between each SL period should be optimized.

It becomes crucial now to perform characterization measurements of the produced photodetectors to obtain a quantitative value of the efficiency. Some figures of merit that will allows to compare the photodetectors are: responsivity (that will give the ratio of the photocurrent generated by the light that reaches the detector), noise, detectivity (that will provide the signal to noise ratio) and the BLIP temperature (that permits to calculate the temperature at which the dark current is equal to the photocurrent caused by background).

6
Bibliography

[1] A. Rogalski, "Infrared detectors: status and trends," *Progress in quantum electronics*, vol. 27, pp. 59–210, 1988. (document), 2.1, 2.1, 2.2

[2] W. Lawson, S. Nielsen, E. Putley, and A. Young, "Preparation and properties of hgte and mixed crystals of hgtecdte," *J. Phys. Chem. Solids*, vol. 9, pp. 325–329, 1959. 1

[3] G. Penello, M. Degani, M. Maialle, M. Pires, and P. Souza, "Photocurrent calculation of intersubband transitions to continuum-localized states in gaas/alas multiquantum wells for mid-infrared photodetectors," *IEEE J.of Qu. Electr.*, vol. 49, pp. 747–752, 2010. 1

[4] W. Herschel, "Experiments on the refrangibility of the invisible rays of the sun," *Philosophical Transactions of the Royal Society of London*, vol. 1, pp. 284–292, 1800. 2.1

[5] T. W. Case, "Notes on the change of resistance of certain substances in light," *Physical Review*, vol. 9, pp. 305–310, 1917. 2.1

[6] A. W. Van-Herwaarden, D. C. Van-Duyn, B. W. Van-Oudheusden, and P. M. Sarro, "Integrated thermopile sensors," *Sensors and Actuators*, vol. 1, pp. 621–630, 1989. 2.1

[7] P. L. Richards, "Bolometers for infrared and millimeter waves," *Journal of Applied Physics*, vol. 76, pp. 1–24, 1994. 2.1

[8] E. Schrodinger, "An undulatory theory of mechanics of atmos and molecules," *Physical Review*, vol. 28, pp. 1049–1070, 1926. 2.2.1

[9] S. Rezende, *Materiais e dispositivos eletronicos*. Sao Paulo: Livraria da Fisica, 2004. 2.2.2

[10] H. Haken, *Light, volume1: waves, photons, atoms*. Amsterdam: North-Holland, 1981. 2.2.4

[11] S. Gasiorowicz, *Quantum physics*. United State of America: Wiley, 1974. 2.2.4

[12] B. F. Levine, C. G. Bethea, K. K. Choi, J. Walker, and R. J. Malik, "New 10 um infrared detector using intersubband absorption in resonant tunneling gaalas superlattices," *Applied Physics Letters*, vol. 50, pp. 1092–1094, 1987. 2.2.5

[13] B. F. Levine, C. G. Bethea, K. K. Choi, J. Walker, and R. J. Malik, "Bound-to-extended state absorption gaas superlattice transport infrared detectors," *Journal of Applied Physics*, vol. 64, pp. 1591–1593, 1988. 2.2.5

[14] C. Sirtoriand, F. Capasso, J. Faist, D. Sivco, S. G. Chu, and A. Cho, "Quantum wells with localized states ate energies above the barrier height," *Applied Physics Letters*, vol. 61, pp. 898–900, 1992. 2.2.5

[15] G. Lenz and J. Salzman, "Bragg confinement of carriers in a quantum barrier," *Applied Physics Letters*, vol. 56, pp. 871–873, 1990. 2.2.5

[16] F. Capasso, C. Sirtori, J. Faist, D. Sivco, S. G. Chu, and A. Cho, "Observation of an electronic bound state above a potencial well," *Nature*, vol. 358, pp. 565–567, 1992. 2.2.5

[17] R. P. Leavitt and J. W. Little, "Infrared photodetectors based on intersubband transition to minigap-confined states in doped quantum wells," *Applied Physics Letters*, vol. 79, pp. 2091–2093, 2001. 2.2.5, 4.4.3

[18] R. P. Leavitt and J. W. Little, "Intersubband transition to minigap-confined states in doped quantum wells," *Infrared physics and technology*, vol. 42, pp. 453–460, 2001. 2.2.5

[19] M. Degani and M. Maialli, "Numerical calculations of the quantum states in semiconductor nanostructures," *Journal of Computational and Theoretical Nanoscience*, vol. 7, pp. 454–473, 2010. 2.3, 4.1

[20] J. M. Cowley, *Diffraction Physics*. The Netherlands: Elsevier, 1995. 3.2

[21] B. S. Instruments, *Rocking Curve Analysis by Dynamical Simulation*. 1990. 3.2

[22] M. A. Capano, K. L. Kavanagh, S. Bensoussan, and L. W. Hobbs, "Analysis of semiconductors by double-crystal x-ray diffractometry," *The Rigaku Journal*, vol. 5, pp. 3–10, 1988. 3.2

[23] N. Kato and S. Tanemura, "Absolute measurement of structure factors with high precision," *Phys. Rev. Lett.*, vol. 19, pp. 22–24, 1967. 3.2

[24] R. H. Fowler and L. Nordheim, "Electron emission in intense electric fields," *Proceedings of the Royal Society of London. Series A*, vol. 119, pp. 173–181, 1928. 3.6

[25] B. F. Levine, "Quantum-wells infrared photodetectors," *Journal of Applied physics*, vol. 74, 1993. 3.6, 4.3.1, 4.3.2

[26] K. K. Choi, *The physics of quantum well infrared photodetectors*. Singapore: World Scientific, 1997. 4.1, 4.3.2

[27] H. Liu, Z. R. Wasilewski, M. Buchanan, and H. Chu, "Segregation of si δ doping in gaas-algaas quantum wells and the cause of the asymmetry in the current-voltage characteristics of intersubband ifraref photodetectors," *Applied Physics Letters*, vol. 63, pp. 761–763, 1993. 4.3.2